NTNU – Trondheim
Norwegian University of
Science and Technology

Investigation of Methods for 2D Strain Imaging of Brain Tumors

Kaja Frøysaa Kvåle

Master of Science in Physics and Mathematics
Submission date: February 2014
Supervisor: Catharina de Lange Davies, IFY
Co-supervisor: Tormod Selbekk, Sintef Teknologi og samfunn
Reidar Brekken, Sintef Teknologi og samfunn

Norwegian University of Science and Technology
Department of Physics

As a student from Biophysics- and Medical technology, I am familiar with the pathological aspects of this project, cancer and tumors, as well as ultrasound theory. The computer programming part on the other hand was not an expertise of mine. Needless to say, this project has been a great challenge for me, but also a great learning experience. The knowledge and experience I have gained from this thesis, is something that I believe I will surely benefit from in my future endeavors.

I would like to start by thanking my supervisors at SINTEF, Tormod Selbekk and Reidar Brekken. Tormod has been my main supervisor and I am grateful that he gave me the opportunity to be a part of the strain imaging project. He has also taught me a lot about strain imaging and brain tumors. Reidar Brekken has been my co-supervisor at SINTEF and I am very thankful for his help with all my computer problems.

Secondly I want to thank my formal supervisor at NTNU, Catharina de Lange Davies, for kindly helping me with my report the past few weeks of the project.

Then I would like to thank former student Thomas Børstad Kristoffersen. Even though he doesn't know it, he has helped me a lot by letting me learn from and be inspired by the program he developed for his Master's thesis in 2011.

Last but not least I would like to thank my family and friends for all their support and motivation through this process, it has meant a lot.

Summary

Intraoperative ultrasound strain imaging displays brain tissue stiffness rather than difference in mass density as regular B-mode imaging. A glioma (the most common type of brain tumor) has a tendency of infiltrating surrounding tissue possibly making it difficult to delineate in a B-mode scan. Complementing B-mode imaging with strain imaging may give additional information about the borders of the tumor thus aiding the surgeons in the task of brain tumor segmentation. It has already been shown that the natural pulsation of the arteries in the brain causes sufficient stress for the displacement in tissue to be measurable with ultrasound.

Strain can be estimated along all three spatial dimensions, but is usually estimated in the direction of propagation of the ultrasound beam. Estimating strain in only one direction does not fully characterize the three dimensional movement of the brain tissue. An improvement is to also estimate the strain in the lateral direction. The reason the strain in the lateral direction is often ignored is due to the poor spatial resolution and the lack of phase information.

Strain is the spatial derivative of a displacement vector or in the case of two-dimensional strain imaging a displacement map generated by a speckle tracking algorithm. The speckle tracking algorithm performs a correlation search to track a two-dimensional kernel through an image series. A correlation coefficient is calculated for every estimate as an indicator of the accuracy of the estimate.

A graphical user interface has been developed to allow the user to change the estimation parameters and view the corresponding results as a cineloop. The displacement estimation is the most time-consuming step of the signal processing chain and makes the method unfit for real-time viewing. Once the displacement is estimated, it is possible to change the strain estimation parameters and see those results in real time thus minimizing the time needed for strain estimation parameter optimization.

The speckle tracking method was tested on simulated ultrasound images with a known displacement and on an elasticity phantom. The developed algorithm estimates the displacement and strain in the axial direction with a high accuracy while the estimates in the lateral direction are noisier. The lateral estimates were expected to be less accurate but the results indicate that there might be an error in the simulated images when the scatterers were displaced laterally.

For the elasticity phantom, the method was only tested on images acquired while the phantom was axially compressed. It is difficult to decide if the lateral strain estimates shown in the images is actual strain or just noise.

The conclusion is that the developed method is able to differentiate structures of different stiffness, but performs better in the axial direction than in the lateral direction, as expected. A better test, and more testing is needed to decide the final performance of the method.

Sammendrag

Intraoperativ ultralyd *strain* avbildning viser hardhet i det avbildede vevet istedet for forskjell i massetetthet, som et vanlig (B-mode) ultralyd bilde gjør. *Strain* eller tøyning kan måles av ultralyd etter en kompresjon av vevet som gjør at stive regioner i et vev vil bevege seg mindre enn myke regioner.

Den vanligste typen hjernesvulst, et glioma, har en sterk tendens til å infiltrere det omliggende vevet, noe som gjør det vanskelig å skille tumor fra friskt vev i et B-mode bilde. Et *strain* bilde kan derfor gi komplementerende informasjon om størrelsen og grensene til tumoren og dermed hjelpe kirurgen med å fjerne mer av tumoren uten å fjerne friskt vev.

Det er vist allerede at den naturlige pulseringen til blodårene i hjerne påfører nok forflytning i vevet til at den er mulig å måle med ultralyd og dermed kan et *strain* bilde produseres.

Strain kan estimeres langs alle romlige akser, men blir vanligvis bare estimert i aksiell retning (bølge-propagasjonsretningen). Det er grunnet at å estimere forflytning av vev i de andre retningene er begrenset av dårlig oppløsning og mangel på et kontinuerlig signal. Et tre-dimensjonalt objekt beveger seg vanligvis i tre dimensjoner. En komponent av bevegelsen er derfor en dårlig karakterisering av den totale bevegelsen. En forbedring er å utvide til to dimensjoner. Det er målet for dette prosjektet.

I to dimensjoner blir *strain* regnet ut som den deriverte av en matrise med forflytningsvektorer. Forflytningsverdiene genereres av en *speckle tracking* algoritme. Algoritmen gjør et korrelasjonssøk mellom et utdrag av et bilde med et større utdrag av det neste bildet i en tids-serie. En forlytningsvektor genereres per søk, i tillegg til en kvalitetsfaktor, korrelasjonskoeffisienten.

Som en hjelp til å anaysere *strain* bildene, ble et *graphical user interface* (GUI) utviklet. GUI'en minsker tiden det tar å optimere *strain* parametrene og lar brukeren se ultralydbildene som en film. Forflytningen tar lengst tid å estimere og gjør derfor metoden uegnet til sanntidsavbildning.

Den utviklede metoden ble testet på simulerte bilder, og ultralyd bilder tatt opp av et elastisitetsfantom. I aksiell retning estimerer metoden forflytning i bildet med god presisjon. I lateral retning er resultatet noe mer usikkert, både fordi det var et problem med de simulerte bildene når lateral forflytning ble indusert og fordi ved avbildning av fantomet var det bare mulig å komprimere fantomet i aksiell retning.

Strain ble estimert ved å bruke sentral differens teoremet.

Konklusjonen er at *speckle tracking* er en god metode for å estimere forflytningsverdiene som brukes til strain estimering i aksiell retning. For å avgjøre hvor godt metoden estimerer forflytning i lateral retning trengs det mer testing av metoden.

Contents

List of Tables

List of Figures

Chapter 1

Introduction

Ultrasound is today one of the most common modalities in the field of medical imaging, it is also considered to be one of the safest. Rather than being based on emitting ionizing radiation through the body, such as computer tomography or X-ray, the ultrasound technique uses high frequency sound waves which to this day has not been proven harmful.

The advantages of ultrasound are the low cost per examination, the equipment which is easy to transport and the real-time acquisition of images which makes it possible to interactively examine the structure but also the functions of organs. There is also no requirement for the building in which the imaging equipment is placed as there is for CT, X-ray and MRI.

While there are several advantages to ultrasound imaging, there are also limitations of the technique such as the limited field of view of the transducer probe, the degradation of image quality due to obesity, the incapability of sound waves to transmit through dense bone and parts of the body which may hold gas such as the bowel and the generally grainy appearance of the image. These disadvantages may make it difficult both to obtain a good quality image and to interpret it. For that a skilled sonographer is required.

What most people probably relate to ultrasound is its use in *obstetrics* (the medical field related to child birth) where an ultrasound scan is used as routine prenatal care to check up on the development of the fetus. While this is a very common use, ultrasound imaging has a number of other applications in various medical fields, both diagnostic and therapeutic, such as in *cardiology* (echocardiography), *gastroenterology* (abdominal sonography) and *urology* (pelvic sonogram). Therapeutic applications include breaking up kidney stones and generation of regional heating and mechanical changes in biological tissue.

A medical field where ultrasound imaging is finding increased application is the field of *neurology*. As mentioned the sound waves are not able to penetrate dense bone therefore imaging through the skull is difficult. There are two options to work around this challenge. The first is imaging the brain through areas where the skull is less dense such as through the temples or the eyes. The second is imaging after a *craniotomy* where a part of the skull has been temporarily removed.

Examples of the former; a transcranial Doppler ultrasound (TCD) is used to estimate

the blood flow of arteries in the brain (Purkayastha and Sorond (2012)), transcranial sonography is a technique used to visualize brain structures, (Walter (2012)) and Jagannathan et al. (2009) describes a technique using high intensity ultrasound as a treatment for brain tumors called transcranial tumor ablation.

An example of the latter is ultrasound imaging of the brain during neurosurgery for tumor removal. Ultrasound imaging is used as a tool to help the surgeons navigate the path to the tumor through brain tissue. A description of ultrasound neuronavigation follows in the next section of this chapter.

1.1 Tumor removal guided by ultrasound

1.1.1 Brain tumors

A tumor is any abnormal mass of tissue. It is the result of the uncontrolled growth and division by one or several cells. Tumors that are located close to the skin surface can often be felt by palpating the skin. They are recognized by their texture that differs from the surrounding tissue. Tumors can be either fluid-filled or hard.

Although a tumor is related to cancer, it is not synonymous with the disease. A tumor may be either benign (non-cancerous) or malignant (cancerous). The difference between them is the ability of a malignant tumor to invade other tissues. A benign tumor is slow growing, has clear borders and is unable to *metastasize* (spread to other parts of the body). It can still cause damage by compressing the surrounding tissue, especially in enclosed spaces such as the brain.

In the brain there are two types of malignant tumors, primary tumors which originated in the brain and secondary tumors (metastatic) that have spread from somewhere else. The most common primary tumor in the brain is the glioma (accumulated from glial cells). The gliomas have a tendency to infiltrate surrounding tissue and it may therefore be hard to delineate their borders.

A malignant brain tumor imposes a great health risk and will eventually lead to the death of the patient if it is left untreated.

1.1.2 Symptoms and diagnosis

The symptoms of a person with a brain tumor will vary depending on its size and location. An abnormal growth in the brain may cause elevated intracranial pressure which leads to physical symptoms like headaches and vomiting. The location of the tumor is the cause of neurological symptoms like degraded memory and loss of motor function. Some patients experience no symptoms at all.

The physician will often request an image of the tumor for the diagnosis. An MR or a CT scan ia the most commonly used imaging modalities because of the clear structural images they provide. The images help the physician determine the position and size of a tumor. If the tumor is malignant a *biopsy* (a sample of the tumorous cells) is performed to characterize the severity of the cancer.

Treating a brain tumor is often a combination of surgery, radiation therapy and chemotherapy. Surgery is often the first step of treatment and the surgeons perform a resection (full

removal) or a partial removal of the tumor if it is located close to a sensitive area. The procedure of tumor removal in the brain is very delicate and complex because of the extreme care that has to be taken not to harm important healthy tissue. To help the surgeons with this, a navigation system using ultrasound is used and a description follows in the next section.

1.1.3 Neuronavigation using ultrasound in brain surgery

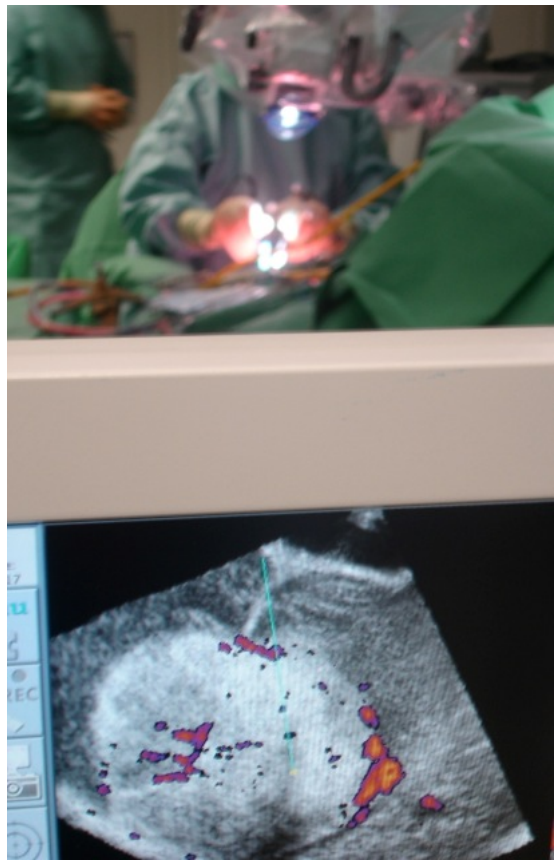

Figure 1.1: Surgeons in the operating room using ultrasound to guide surgery. The ultrasound image shows a tumor and the blue line is an example of the surgeon using the pointer tool to locate a structure in the brain.

Due to the situation described above a lot of planning goes into the treatment of a brain tumor. An MR scan is acquired to decide the exact anatomical position of the tumor and functional MRI (fMRI) or diffusion tensor imaging (DTI) is used to create a map of the neurological paths in the area. These images aid in the planning of the best path to reach the tumor without damaging areas of the brain associated with key functions.

During the surgery the previously acquired MR scan is used as a structural map of the brain to locate the tumor. To navigate this map the surgeons at St. Olavs hospital (Trondheim, Norway) use a system provided by SonoWand (SonoWand AS, Trondheim, Norway). The navigation system is equipped with a pointer tool that the surgeon can point anywhere inside or near the brain and its position will show up on the MR scan. An example of the system in use in an operating room is shown in figure 1.1.

As the surgery proceeds the brain tissue might be displaced by surgical retraction, the resection cavity itself or shifts in brain tissue caused by leakage of cerebrospinal fluid. These effects cause the MR scan to become a less accurate map of the current situation. Therefore ultrasound is used to gain updated information on the remainings and position of the tumor. The ultrasound scan is acquired after craniotomy but before resection of the tumor. The surgeon will periodically acquire ultrasound scans to detect if there has been any change in the position of the tumor.

Many hospitals use conventional (B-mode) ultrasound imaging during brain surgery but due to the fact that tumors, glial tumors especially, have a similar visual appearance to normal brain tissue (Chakraborty et al. (2012)) the borders of a tumor and the remainings of the tumorous tissue after surgery may be difficult to detect in a B-mode scan. Solheim et al. (2010) investigated the use of B-mode images during surgery and the effects it had on the outcome of patients over the course of three years. The article reports that the ultrasound B-mode images and MR images found very little agreement on the sharpness of the tumor borders and the sizes of the lesions. Due to, among others, these challenges it is natural to look for imaging techniques that can give a better image of the tumor borders and size. This is one of the main motivations behind this thesis.

1.2 Goal and motivation of thesis

A conventional ultrasound image (B-mode) displays the different densities of the insonated tissue. The brightness of a pixel is decided by the intensity of the echo reflected from an interface between two types of tissue. The stronger the echo, the brighter the pixel. If processed in a different way, it is possible to extract other types of information from the signals. Values of tissue or blood motion is calculated from the signals when using *Doppler imaging*.

Strain imaging is an imaging technique dedicated to displaying tissue hardness through calculating the displacement of tissue under stress. In general, tissues are differentiated in a strain image because when subjected to a uniform force a hard material will displace less than a softer material.

It was reported by Ophir et al. (1999) that tissue stiffness in general is uncorrelated with echo strength, thus it is probable that complementary information about the imaged tissue can be gained from strain imaging. As mentioned above, Chakraborty et al. (2012) found that tumors may a similar visual appearance to normal tissue and Souchon et al. (2003) reported that tumorous tissue in general is stiffer than healthy tissue. This implies that for brain tumors especially, *strain imaging* may be helpful.

The National centre for ultrasound and image-guided surgery (collaboration SINTEF/NTNU/St. Olavs) and my advisor and co-advisor Tormod Selbekk and Reidar Brekken, have already shown that it is possible to generate strain images of brain tumors by detecting the tissue displacements that are introduced by the normal arterial pulsation in the brain (Selbekk et al. (2010, 2005)).

A limitation in the previous published work is that strain is only estimated in the axial direction of the image plane. Displacement in tissue under stress is likely to be three-dimensional thus the strain in one direction does not fully describe the motion nor the mechanical properties of a three dimensional target. A more complete characterization of the brain tissue could possibly help in guiding a safer surgery. This is the key motivation behind this project.

The aim of this project is to explore methods for estimating the displacement and strain of tissue in two dimensions, both the axial and the lateral directions. In 2010 a former student, Børstad (2011), implemented a solution to the axial strain problem for his Master's thesis. This project is a continuation of his work.

Three goals were set up for this project:

1. Investigate different previously published methods for estimation of 2D strain (axial, lateral).
2. Implement methods for 2D strain estimation in Matlab.
3. Evaluate the performance based on synthetic data and experiments with an elasticity phantom.

Chapter 2

Basic Theory

As an introduction to the field of ultrasound imaging the first section of this chapter will present some of the basics of image formation and the most important factors of image quality.

The next section will present *elastography* and strain imaging. The typical signal processing chain in strain imaging is the estimation of displacement in a material under stress followed by the calculation of strain from the displacement estimates. Even though displacement comes first in the signal processing chain, the properties of strain and strain imaging is presented first.

2.1 Basics of ultrasound image formation

Medical ultrasound is a pulsed-echo technique based on transmitting inaudible sound waves through tissue and receiving the echoed events from tissue interfaces or small scattering objects. The frequency of the ultrasound waves are typically in the range of 2 to 20MHz while the audible range is around 20 to 20 000Hz. The wavelength of ultrasound, λ, is inversely related to the velocity of sound, c,

$$c = \lambda f. \tag{2.1}$$

The velocity of sound is constant at a given temperature but varies depending on the properties of the material it is propagating in with the relation,

$$c = \sqrt{\frac{\kappa}{\rho}}, \tag{2.2}$$

where κ is the bulk modulus of elasticity and ρ is the mass density of the material.

Reflection and scattering A typical biologic material is often inhomogeneous. This means that the material is composed of several types of tissues with different acoustic properties. Equation 2.2 shows that the speed of sound is tissue specific and will vary slightly throughout a biologic material. For soft tissues (fat excluded) the variation is negligible and the velocity is considered to be constant at $1540m/s$.

What creates the contrast in the ultrasound images is the differences in acoustic impedance, Z. Z is related to the density of the material, ρ, and the speed of sound,

$$Z = \rho \times c = \sqrt{\frac{\rho}{\kappa}}. \tag{2.3}$$

When the ultrasound hits an interface between two tissues with different Z some of the wave will be reflected and some of the wave is transmitted. How large the difference of Z is decides how much of the wave is reflected. For example, an interface between soft tissues typically leads to a reflection of 1%, while boundaries between soft tissue and bone reflects $10 - 20\%$ of the intensity of the original beam. As sound waves are almost incapable of propagating through gas and dense bone an interface with either of these materials leads to almost total reflection and creates an acoustic shadow in the image (Prof. Bjørn A. J. Angelsen (2010)). The intensity of the reflection decides the amplitude and thus the brightness of the pixel in the b-mode image.

The intensity of the reflection is defined by the reflection coefficient, R, as the ratio of the incoming, Z_1, and reflected, Z_2, amplitudes (Prof. Bjørn A. J. Angelsen (2010)),

$$R = \frac{Z_2 - Z_1}{Z_1 + Z_2} = \frac{\rho_2 c_2 - \rho_1 c_1}{\rho_1 c_1 + \rho_2 c_2}. \tag{2.4}$$

The position of a particular echo in the b-mode image is decided by the time emission to receive of a pulse, t,

$$t = \frac{2d}{c}, \tag{2.5}$$

where d is the depth of the reflecting incidence, c the speed of sound and 2 is for the distance from the transducer and back. The time of sampling is detected by the ultrasound system and the depth calculated from equation 2.5 as

$$d = \frac{tc}{2}. \tag{2.6}$$

Not all of the energy from the transmitted pulses is returned to the probe. Reflection does not only happen at tissue interfaces, small objects, compared to the λ, will scatter some of the energy in all directions. These objects are referred to as scatterers. Most tissue surfaces are not completely smooth and the roughness of the surface scatters adds a scattered component to the reflected wave, making the reflection *diffuse* ((Prof. Bjørn A. J. Angelsen, 2010, p 1.21)).

Attenuation and time gain compensation (TGC) The amplitude of the ultrasound beam decreases with depth due to attenuation. There are three factors contributing to the attenuation, the main factor is conversion of absorbed wave energy to heat. The second factor is due to reflection and scattering. The third is due to the divergence of the beam. Additional attenuation is found in the diverging regions of the beam ((Prof. Bjørn A. J. Angelsen, 2010, p 1.23)). The absorption attenuation is dependent on the intensity absorption coefficient μ(f) which is a function of the transmit frequency of the pulse. Attenuation is measured in [dB/cmMHz], the attenuation in human tissue is approximately 0.5 [dB/cmMHz] one way.

The attenuation makes the reflection from targets deep in the tissue weaker than reflections from shallow targets. The receiver amplifier in the ultrasound system compensates for this using a time variable gain. When the signal from the deep targets is amplified so is the noise.

The absorption and scattering increases when the frequency increases, thus to penetrate deeper into the tissue a lower frequency is favorable.

Transducer and beamforming The hardware of an ultrasound system consists of a electric pulse generating scanner and a transducer that converts the electrical pulses into mechanical oscillations. The transducer consists of one or several crystals of a piezo-eletric material. This material starts to oscillate in thickness when an electric pulse is applied and generates electric pulses when subjected to mechanical oscillations.

A phased array transducer consists of several transducer elements in a row. The length of this row is the footprint of the transducer and for a linear array is also the image width. These elements are activated individually to emit a beam in a specific order which creates a beam that is steered in a direction because of the positive interference that results from the partial waves of each element. This is called electronic steering. The beam can be electronically focused at a specific depth as well using time delays.

When an image is used in a clinical setting it is important that it is possible to distinguish between different structures and that the structures shown in the image are of the actual tissue and not image artefacts. Some factors of image quality will be presented in the next section.

2.1.1 Factors of image quality

The performance of a medical imaging modality is usually decided by three main factors: the spatial resolution, contrast resolution and temporal resolution ((Prof. Bjørn A. J. Angelsen, 2010, p 1.44)).

Resolution *Spatial resolution* is a measure of the system's ability to differentiate between closely located structures and it is limited by the *point spread function* (PSF) of the system. The PSF of the system decides how much a point target will be smeared out in the image. The spatial resolution is defined along three axes. Axial direction is along the

direction of wave propagation, lateral direction is the beam scan direction and the elevational direction is perpendicular to both the axial and lateral directions.

Axial resolution is the minimum distance at which two points can be located (along the propagation direction) and still be observed as separate structures in the image. The length of the transmitted pulse decides the axial resolution. The pulse length, T_p is a function of the number of pulse cycles, n and the period, T of the transmitted pulse, $T_p = nT$. The axial resolution can be expressed as

$$\Delta z = c \times \frac{T_p}{2} = c \times \frac{nT}{2} = \frac{n\lambda}{2}, \tag{2.7}$$

where $\lambda = \frac{c}{f} = cT$, from equation 2.1. Equation 2.7 shows that the axial resolution depends on the frequency, by increasing the frequency the resolution is increased.

Lateral resolution is the minimum distance at which two points at the same depth can be located and still be observed as separate structures. Lateral resolution is mainly decided by the width of the beam, Δl,

$$\Delta l = \frac{\lambda F}{D} = \frac{c}{f}\frac{F}{D}, \tag{2.8}$$

((Prof. Bjørn A. J. Angelsen, 2010, p 1.14)), where F is the focal depth and D the transducer aperture. Equation 2.8 shows that the lateral resolution is inversely related to the frequency, thus increasing the frequency also increases lateral resolution. When several point targets are located closely enough to be covered by one beam width the scattered signals from the targets create an interference pattern in the image called speckle pattern.

The resolution in the elevational direction or the slice thickness resolution which it is often referred to is decided by the height of the transducer elements.

The spatial sampling frequency is much coarser in the lateral direction than in axial. The axial resolution is therefore much greater than the lateral resolution which makes the latter the limiting factor of the spatial resolution of the system.

Contrast resolution is a measure of the systems capability to distinguish between structures with small variations in the intensity of the backscattered signal that are located nearby each other. The main cause of degrading of contrast resolution is signal generated noise Prof. Bjørn A. J. Angelsen (2010), caused by side lobes and reverberations.

Temporal resolution is the frame rate, F, equal to the number of images acquired per second. For an image with N beams and time per beam, T_b, the time it takes to generate one image is $T = N \times T_b$. The time per beam depends on the depth, d, of the objects to be imaged and the speed of sound. It will take at least $\frac{2d}{c}$ seconds for the pulse to return from the deepest target, and to be sure that the previous pulse is sufficiently attenuated another period of time, T_0 is added to the waiting time. This leads to the frame rate,

$$framerate = \frac{1}{T} = \frac{1}{NT_b} = \frac{1}{N(2\frac{d}{c} + T_0)}, \tag{2.9}$$

((Prof. Bjørn A. J. Angelsen, 2010, 0. 1.30)).

Reverberations is a phenomenon of multiple reflections. In principle a pulse is caught between two targets scattering back and forth until it loses its energy, creating several echoes from one target.

Apodization Apodization is a method to reduce the side lobes of the ultrasound beam by increasing the width of the main beam. Side lobes are additional unwanted side beams to the main beam, which cause reflections from outside the image plane and therefore artefacts in the image.

Apodization gradually decreases the vibration of the transducer surface with respect to the center of the transducer. This is accomplished by using more power to excite the central elements. Reducing the size of the transducer elements improves the apodization.

2.1.2 Imaging techniques

The simplest of ultrasound imaging techniques is the *A-mode*. The *A* stands for amplitude and the returned signal is displayed with the horizontal axis as the time from transmission to receive and with the vertical axis as the strength of the echo.

A two dimensional image of tissue structure is called a *B-mode* image. The *B* stands for brightness because the strength of the amplitudes of the signals is displayed as differences in grayscale values.

An *M-mode* image, *M* for motion, is a time-series of A-lines acquired from the same position with the amplitudes displayed as brightness values. M-mode is used to analyze the movement of a specific structure by taking advantage of the fact that reflections from an axially moving structure will change in depth through time. The movement will often be displayed as an oscillating curve in the M-mode display and it is possible to calculate movement and displacement of the particular organ of interest.

Doppler imaging is a functional imaging method rather than a structural method as the ones mentioned above. With Doppler imaging it is possible to visualize the movement of blood or tissue. The method takes advantage of the Doppler frequency shift between two objects moving relative to one another. The shift is given by the Doppler equation,

$$f_d = 2f_0 \frac{vcos\theta}{c}, \tag{2.10}$$

where f_0 is the frequency of the transmitted signal that is reflected from an object moving with velocity v at an angle θ relative to the direction of the ultrasound beam. The values from Doppler imaging are usually displayed with the B-mode image as background

and with either velocity (Color Doppler) or the power of the signal (Power Doppler) displayed as color encoded values. Only the axial velocity component is measured, while the actual velocity vector might be three-dimensional.

Ultrasound elastography is another functional imaging technique that assesses the elasticity and strain of tissue. The technique is based on applying some kind of stress or force on tissue and observing the resulting movement. The term elastography was first presented by Ophir et al. (1991), where the author focused on applying a uniform axial stress on the tissue.

Since then elastography has become a collective term for many different techniques. The largest difference among them is based on the method of tissue excitation. The applied stress can be either external (from manually compressing the tissue or an electric vibration device) or internal (from the natural pulsation of arteries or active organs like the heart or the lungs). Some techniques are based on the acoustic radiation force of the propagating ultrasound wave to induce movement in the tissue. A map over the different approaches to elastography can be found in Parker et al. (2011).

2.2 Strain imaging

After a deformation in one direction of a segment of length L_0, the strain (ε) in that direction is defined as

$$\varepsilon = \frac{\Delta L}{L_0} = \frac{l - L_0}{L_0} \tag{2.11}$$

where l is the length of the segment after deformation. ε is sometimes referred to as engineering strain or Cauchy strain. Strain is a dimensionless property and is often expressed in per cent or per mille.

The magnitude of strain is dependent on the elasticity of the material and the strength of the applied force. Elasticity is the ability of a material to resume its original shape and size after being subjected to some kind of stress or deforming force. Stress (σ) is defined as the force applied per unit area,

$$\sigma = \frac{force}{area} = \frac{F}{A}. \tag{2.12}$$

A very elastic material will be displaced more than a stiffer material, meaning the softer material strain more than the stiff material, see figure 2.1.

The strain of a single segment of tissue does not hold a lot of information. In fact, because strain is dependent on both the strength of the applied force and the elasticity of the material, strain is not a true elastic property. Strain alone cannot characterize a material but a local map of strain values could be of clinical value if the area were to be compressed by a uniform force. The local deformations would then show the differences in elasticity in the tissue, and could point to an abnormality in the tissue if the strain values were to show abnormal values.

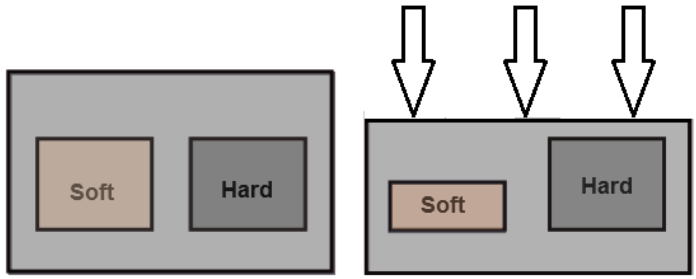

Figure 2.1: When compressed in the same direction by the same magnitude of force, a stiff material will be less affected than a softer material. This means that the change of initial length in the stiff material will be less changed after compression than the length of the soft material, thus the stiff material will strain less, see equation 2.11.

Young's modulus on the other hand is a measure of elasticity of a material. It is a value that characterizes tissue and could therefore be used to compare tissue characteristics of different patients.

Young's modulus, E, is the constant ratio $stress/strain$ and has the unit Nm^{-2}. Combining equations 2.11 and 2.12 Young's modulus can be defined as

$$E = \frac{\sigma}{\varepsilon} = \frac{\frac{F}{A}}{\frac{\Delta L}{L_0}} = \frac{FL_0}{a\Delta L} \tag{2.13}$$

Rearranging equation 2.13

$$F = (\frac{EA}{L_0})\Delta L = kx, \tag{2.14}$$

where F is the force exerted by the material when it is deformed by a length ΔL. This in turn can be used to derive *Hooke's law* which describes the stiffness of a perfect spring. k is the stiffness parameter characteristic for the spring and x is the distance the spring is compressed.

It is worth mentioning again that although strain imaging does not reconstruct the Young's modulus, it can still be useful in a clinical setting.

- If the stress applied to the tissue is due to natural pulsation, abnormal strain values could potentially indicate an abnormality in the tissue.
- When a uniform force is applied to a material, the different elastic properties of the material will show through strain.

Two-dimensional strain

For a two-dimensional displacement the strain tensor is defined as

$$\varepsilon_{\text{ij}} = \frac{1}{2}(\frac{\partial u_i}{\partial x_j} + \frac{\partial u_j}{\partial x_j}), \tag{2.15}$$

where x_i are the coordinates, u_i are the estimated displacements and ε_{ij} are the various strain components. The indices i and j represent the axial and lateral directions, respectively, Techavipoo et al. (2004).

All strain components can be deduced when both displacement vectors are known (see equation 2.15), but estimating strain is often limited to the axial direction. The reason is that the lateral displacement vector is more difficult to obtain.

2.3 Displacement based strain estimation

From equation 2.11 the strain of a segment in on direction is calculated as the change in length of a segment after a compression, divided by the initial length of the segment. Or defined as the derivative of a length segment as in equation 2.15.

If an axial segment is considered to be along a scan line centered at depth *m*. Then the endpoints for that segment are located in $m_l = m + [\Delta m/2]$ where the subscript *l* stands for *lower* meaning furthest from the transducer, and $m_u = m - [\Delta m/2]$ where *u* stands for *upper* meaning closest to the transducer. For a segment defined in this way, the strain can be calculated using finite difference theory:

$$f'(m) = \frac{f(m + \frac{\Delta m}{2}) - f(m - \frac{\Delta m}{2})}{2\frac{\Delta m}{2}} = \frac{f(m + \frac{\Delta m}{2}) - f(m - \frac{\Delta m}{2})}{\Delta m} = \varepsilon, \tag{2.16}$$

where Δm is the length of the segment in depth samples.

The lateral strain is calculated in the same way, only the segment is a vertical vector centered at line *n*, with endpoints in $n_r = n + [\Delta n/2]$ where *r* stands for *right* and $n_l = n - [\Delta n/2]$ where *l* stands for *left*.

The central difference strain estimator A strain image is generated from a matrix of local displacement estimates, $\hat{D}(m, n)$. Thus using equation 2.16, axial strain can be calculated as

$$\hat{\varepsilon}[m, n] = \frac{\hat{D}[m_l, n] - \hat{D}[m_u, n]}{\Delta m}. \tag{2.17}$$

Lateral strain is can be calculated as

$$\hat{\varepsilon}[m, n] = \frac{\hat{D}[m, n_r] - \hat{D}[m, n_l]}{\Delta n}. \tag{2.18}$$

If Δm and Δn are even numbers. A strain image when the strain estimates are represented by color or gray-scale values is usually referred to as an *elastogram*.

2.4 Two-dimensional displacement estimation

Displacement is more difficult to estimate in the lateral direction compared to the axial direction due to two main reasons:

- The resolution in the lateral direction is much poorer than in the axial direction which leads to much noisier lateral estimates.

- While axial motion can be estimated either by the shift in baseband phase or by time-delay estimation, there is no radiofrequency phase information in the lateral direction and a different approach must be used.

The drawbacks of only estimating the axial component are first of all that the motion of a tissue under stress is most likely to be three-dimensional, thus the axial component of motion does not provide the full characterization of the movement. Secondly, the lateral and elevational motion lowers the accuracy of the axial estimates by decorrelating the signal, (Konofagou and Ophir (1998)).

2.4.1 Mathematical notation

The ultrasound echoes are sampled as they reach the receiving transducer. The ultrasound data from the scanner is called RF(radio-frequency)-data. The RF-data is a two-dimensional matrix with the rows defined as the sampled depth signal (one A-line), and the columns the number of A-lines acquired for one image. One ultrasound frame is a rectangular two-dimensional matrix with **M** depth samples, **N** lateral scan lines in a time-series with **O** frames. Each sample is represented by the coordinates $[m, n, o]$ in time-space. The displacement is estimated between two frames, often between two subsequent frames, o and $o + 1$.

The sample value of a typical signal is represented as $x[n]$, where n is the range value of the signal. The RF samples are represented by three range values, the depth range n, the scan line range m and the time-frame range, o. The real and discrete representation of the three dimensional RF signal is thus x[m,n,o]. The depth index, m, is ordered from the transducer surface with increasing depth, the scan lines are ordered in the direction of image acquisition, from left to right in the transducer frame of reference. The frames are ordered with increasing time.

The time-series can be represented as a set of **O** matrices with one frame represented as $X_{\text{frame number}}$,

$$X_0 = \begin{bmatrix} x[0,0,0] & x[0,1,0] & \cdots & x[0,N-1,0] \\ x[1,0,0] & x[1,1,0] & \cdots & x[1,N-1,0] \\ \vdots & \vdots & \ddots & \vdots \\ x[M-1,0,0] & x[M-1,1,0] & \cdots & x[M-1,N-1,0] \end{bmatrix}$$

$$X_{\text{O-1}} = \begin{bmatrix} x[0,0,O-1] & x[0,1,O-1] & \cdots & x[0,N-1,O-1] \\ x[1,0,O-1] & x[1,1,O-1] & \cdots & x[1,N-1,O-1] \\ \vdots & \vdots & \ddots & \vdots \\ x[M-1,0,O-1] & x[M-1,1,O-1] & \cdots & x[M-1,N-1,O-1] \end{bmatrix} \tag{2.19}$$

The notation is taken from Børstad (2011).

2.4.2 Axial displacement estimation

Movement of the scatterers in between acquisition will result in the returned echoes being either closer or further away from the transducer in the second A-line. The movement of scatterers results in both a phase and a time-shift compared to the initial A-line. That leads to two estimation techniques: time-domain technique (cross-correlator) and phase-domain technique (autocorrelator).

Correlation based time-delay estimation (TDE): A new method for estimating axial displacement was suggested by Ophir et al. (1991). The method evaluates time-shift between two A-lines acquired at the same location but at different states of deformation. The shift is detected by extracting a segment of echoes from the first A-line and translating this segment across the second A-line to compare the similarity of the two segments using cross-correlation. The peak value of the cross-correlation function indicates the new position of the segment.

Phase-domain technique: The cross-correlation function of two ultrasound RF signals $x_1(t)$ and $x_2(t)$ is

$$R_{12} = E[x_1^*(t)x_2(t+\tau)], \tag{2.20}$$

where $E[]$ is the statistical expectation operator, t is the time and τ the time shift between the two signals.

An analytic ultrasound signal can be expressed as

$$x(t) = A(t)e^{j\omega_c t}, \tag{2.21}$$

where $A(t)$ is the ultrasound pulse envelope, ω_c is the angular carrier frequency.

Using equation 2.21 in equation 2.20 for an analytic signal $x_1(t)$ and a time-delayed version of $x_1(t)$, $x_2(t-t_d)$ where t_d is delay the correlation function can be expressed as

$$R_{12}(t,\tau) = e^{j\omega_c(\tau - t_d)}|R_{11}(t,\tau - t_d)|, \tag{2.22}$$

where R_{11} is the autocorrelation function of $x_1(t)$. is the magnitude operator. Equation 2.22 shows that the cross-correlation function is a time-shifted version of the autocorrelation function. The phase of the function crosses zero where the magnitude reaches maximum. This is the basis of the phased-based zero crossing method. It can only be used in the axial direction due to the carrier frequency of the signal which is only available in the axial direction.

Thus there are two major limitations in lateral displacement estimation compared to axial displacement estimation: the first is the lack of a continuous signal and phase information and the second is the poor resolution in the lateral direction compared to the axial direction. The latter makes the lateral estimates much noisier than the axial estimates. A description of a two-dimensional estimation technique follows in the next section.

2.4.3 Speckle Tracking

Speckle tracking was originally created as an alternative or an improvement of the well-known Doppler method for quantifying and imaging blood velocity or tissue motion. The method was first reported in an article by Trahey et al. (1987) and is called speckle tracking, but in reality the algorithm could track any constant pattern.

The technique is similar to the TDE method used for axial displacement estimation in the way that a template segment is translated across a region of interest searching for the best match. The main difference is that the segment used in speckle tracking is a two-dimensional array and the search is performed within a two-dimensional search region allowing for movement to be estimated in axial and lateral direction. The searching algorithm is also called a block matching algorithm, Hein and O'Brien (1993), because a block of the image is extracted and used as the template in the search.

What is a speckle pattern?

Speckle is the natural background in a B-mode ultrasound image. When two small objects are located closely enough to be covered by the same pulse, the reflection from these scatterers will interfere and create a pattern of negative or positive interference, [TTK4160 p.1.28]. If several scatterers are covered by the same pulse they create a pattern which has a more rapid spatial variation than a pattern from individual scatterers. This pattern is called a speckle pattern and may be mistaken as a real tissue structure in the image.

The speckle pattern is useful in pattern tracking due to:

1. The randomness of the scatterers ensures that the speckle pattern has a unique composition which makes it useful for differentiating one region from another.

2. The displacement in elastography is so small that the speckle pattern remains sufficiently stable during deformation,Wells and Liang (2011).

The creation of speckle is illustrated in figure 2.2 a and b.

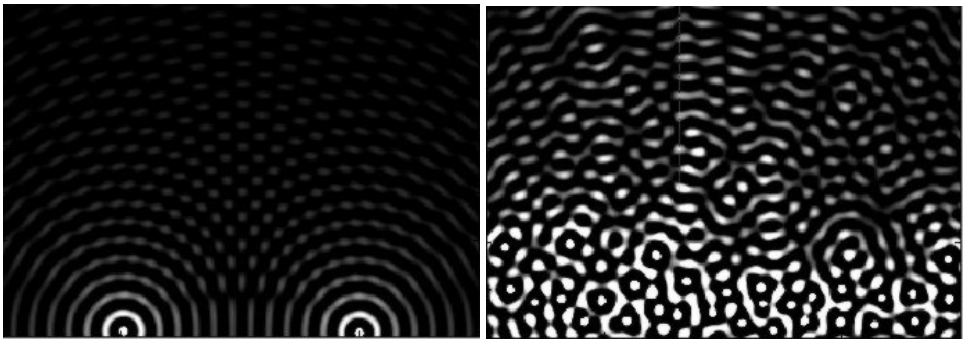

(a) Interference from two scatterers. **(b)** Interference pattern from multiple scatterers.

Figure 2.2: Speckle pattern from a) two scatterers and b) several randomly distributed scatterers. The images are reproduced with permission from: (http://folk.ntnu.no/stoylen/strainrate)

Advantages of speckle tracking over Doppler imaging

There are two major limitations of Doppler velocity estimation. The method is angle dependent and the limitation on the range of detected velocities before aliasing occurs. Doppler imaging calculates velocity from the phase change that happens when a signal is returned from a moving target. Rearranging equation 2.10

$$v_a = vcos\theta = \frac{cf_s}{2f_0} \tag{2.23}$$

shows the angle dependency of the Doppler velocity estimate. Regardless of the direction of motion of a target only the axial velocity component is calculated. The maximum velocity of a moving target before aliasing occurs is defined by the pulse repetition frequency (PRF) which is equal to the sampling frequency f_s for pulsed Doppler, **?**. PRF is equal to $1/T_s$, where $T_s = 2D/c$ is the time between transmitted pulses and D the depth of the target.
To avoid frequency aliasing the Doppler shift needs to be less than half the sampling frequency,

$$f_d > \frac{PRF}{2} = \frac{f_s}{2}. \tag{2.24}$$

Combining equation 2.10 and 2.24 the maximum detectable velocity is

$$v = \frac{c^2}{8Df_0}. \tag{2.25}$$

The speckle tracking method directly tracks the echoes produced by the ultrasonic scatterers in the tissue by finding that same speckle pattern in the subsequent frame. The pattern can be found in any direction from the starting point making the speckle tracking method two-dimensional and thereby overcoming the angle dependency of Doppler imaging. Instead of calculating velocity the speckle tracking method tracks displacement values and frequency aliasing is not a problem for this method.

Mathematical notation

The matrices in equation 2.19 show the mathematical representation of the RF data in a time-series. The kernel is a subset of samples with l axial samples and k lines, centered around the point, $p(m, n)$, for which the movement is tracked,

$$K_t = \begin{bmatrix} x[m-\frac{l}{2}, n-\frac{k}{2}, t] & x[m-\frac{l}{2}, n-\frac{k}{2}+1, t] & \cdots & x[m-\frac{l}{2}, n+\frac{k}{2}, t] \\ x[m-\frac{l}{2}+1, n-\frac{k}{2}, t] & x[m-\frac{l}{2}+1, n-\frac{k}{2}+1, t] & \cdots & x[m-\frac{l}{2}+1, n+\frac{k}{2}, t] \\ \vdots & \ddots & \vdots & \\ x[m+\frac{l}{2}, n-\frac{k}{2}, t] & x[m+\frac{l}{2}, n-\frac{k}{2}+1, t] & \cdots & x[m+\frac{l}{2}, n+\frac{k}{2}, t] \end{bmatrix} \tag{2.26}$$

The search region is a larger subset of samples with i samples and j lines from a subsequent time frame centered around the same point, the size of the search region defines the maximum expected displacement,

$$S_{\text{t+1}} = \begin{bmatrix} x[m-\frac{i}{2}, n-(\frac{j}{2}), t] & x[m-\frac{i}{2}, n-\frac{j}{2}+1, t] & \cdots & x[m-\frac{i}{2}, n+\frac{j}{2}+1, t] \\ x[m-\frac{i}{2}+1, n-\frac{j}{2}, t] & x[m-\frac{i}{2}+1, n-\frac{j}{2}+1, t] & \cdots & x[m-\frac{i}{2}+1, n+\frac{j}{2}, t] \\ \vdots & \vdots & \ddots & \vdots \\ x[m+\frac{i}{2}, n-\frac{j}{2}, t] & x[m+\frac{i}{2}, n-\frac{j}{2}+1, t] & \cdots & x[m+\frac{i}{2}, n+\frac{j}{2}, t] \end{bmatrix} \tag{2.27}$$

If a full search is performed the kernel is placed in the corner of the search region and translated sample by sample until the whole region has been covered. A normalized correlation coefficient, $\rho_{x,z}$ is calculated for every translation as a measure of similarity between the kernels.

Normalized cross-correlation (NXC):

$$\rho_{x,z} = \frac{\sum_{i=1}^{k}\sum_{j=1}^{l}(K_{i,j}-\bar{K})(S_{i+x,j+z}-\bar{S})}{\sqrt{\sum_{i=1}^{k}\sum_{j=1}^{l}[K_{i,j}-\bar{K}]^2 \sum_{i=1}^{k}\sum_{j=1}^{l}[S_{i+x,j+z}-\bar{S}]^2}}, \tag{2.28}$$

where x, z is the lag (displaced position within the search region), X is the kernel in the first image and Y is the search region in the subsequent image. The normalized cross-

correlation function generates values between -1 and 1. 1 is a complete similarity, -1 is a complete opposite.

The full search produces an array of correlation coefficients. The number of times the kernel can fit within the search region without crossing its borders determines the size of the correlation coefficient matrix,

$$CC = \begin{bmatrix} \rho[z_1 1, x_1 1] & \rho[z_1 2, x_1 2] & \cdots & \cdots \\ \rho[z_2 1, z_2 1] & \rho[z_2 2, x_2 2] & \cdots & \cdots \\ \vdots & \vdots & \ddots & \vdots \\ \cdots & \cdots & \cdots & \cdots \end{bmatrix} \tag{2.29}$$

The displacement is found from the position of the highest correlation coefficient.

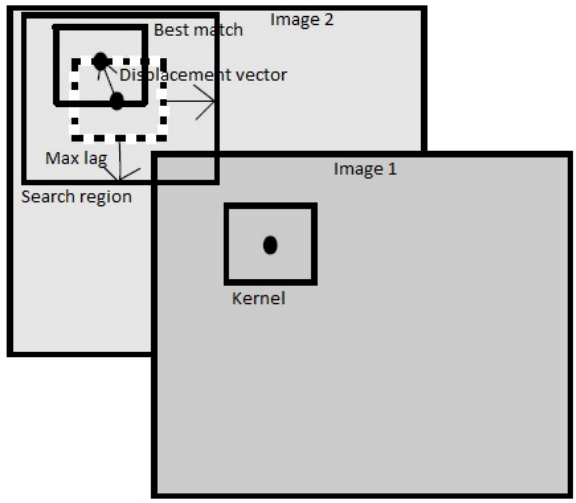

Figure 2.3: A kernel is defined around a center point in image 1. A search region is defined around the same center point in a subsequent frame (image 2). The displacement of the kernel from image 1 to image 2 is estimated by performing a normalized correlation search. The kernel is translated over every possible configuration within the search region and a correlation coefficient is calculated for every single translation. The peak value amongst the correlation coefficients indicates the new location of the kernel and the distance from the position of the center point in image 1 to the position of the center point in image 2, is the displacement vector, which can be decomposed into a z- and an x-component, thereby making the search a two-dimensional correlation search.

B-mode data vs RF-data

Speckle tracking has been documented using both B-mode data and RF-data. In Trahey et al. (1988) the authors used RF-data for blood velocity estimation, but Trahey et al. (1987) used B-mode data. The reason for using B-mode data in the latter was to remove the cyclic nature of the RF-data to remove aliasing.

Other studies (Bohs et al. (2000)), argue that RF-data gives more accurate results if the sampling frequency in the axial direction is large enough. RF-data does contain more information than B-mode data. In B-mode data only the amplitudes of the signals are kept while the RF-data also contains phase information.

Size of kernel

The size of the kernel is a trade-off between resolution and robustness. A large kernel gives a more unique pattern making it easier to track, but when choosing a kernel an assumption that the whole area of the kernel has moved with the same velocity is made, which may not be true. Thus using a large kernel size, the displacement estimates will be more uniform due to the averaging over a large array of samples.

Size of search region

The size of the search region limits the expected displacement of the point. If the true displacement is larger than the search region the algorithm will give a faulty displacement estimate. A large search region gives the benefit of not excluding displacement distances, but increases the risk of finding several correlation peaks. A small search is probably more accurate if the displacement is within the set limits.

Computational complexity

Cross-correlation is a computationally expensive procedure. A number of other pattern matching algorithms have been suggested to improve the efficiency and time of the search. Sum of absolute differences (SAD) measures the similarity between two kernels by taking the absolute difference of each sample in two different states of deformation and summing these values. The position with the lowest sum of absolute difference indicates the new position of the kernel.

Normalized cross correlation is said to yield optimal estimates.

2.5 Other methods for estimating lateral displacement

Following below is a short introduction to other methods that were found relevant for lateral displacement estimation but not used in this project. The field of lateral displacement estimation contains a large number of existing methods, many of them similar to already existing techniques but with small improvements added. The methods presented here have a fundamentally different approach to the problem and have therefore been chosen for this short overview of some of the existing methods.

2.5.1 Synthetic lateral phase (SLP)

A method was proposed by Chen et al. (2004) to overcome the lack of phase information in the lateral direction. The proposed solution is to create a synthetic lateral phase by eliminating one half of the lateral frequency spectrum of the analytic signal. When either

the positive or negative spectrum is reconstructed by inverse the Fourier transform the signal contains a synthetic lateral phase. A synthetic lateral phase allows for the zero-crossing method used for axial displacements to be applied also in the lateral direction.

Because the spectrum is symmetric with respect to zero frequency, all the information is preserved in either half of the lateral spectrum. The final purpose of this method is to provide a more accurate lateral displacement estimate. Speckle tracking is used to find the displacement estimates.

The first step of the algorithm: creation of the synthetic phase in the lateral direction by splitting the spectrum of the analytic signal with respect to zero frequency in the lateral direction into up and down halves. By choosing to reconstruct either half of the lateral spectrum, the signal is no longer centered around zero frequency. This is what makes the phase available in the lateral direction.

The second step of the algorithm: calculation of the correlation functions in axial and lateral directions between two RF-frames. A scheme called double zero crossing is applied to the correlation functions to detect the phase zero crossings in both directions.

Amar et al. (2011) used this method for brain strain estimation.

2.5.2 RF-methods

Konofagou and Ophir (1998) proposed a new method for lateral displacement estimation with the highest precision possible. The method proposes to estimate the Poisson's ratio, $\nu = -\frac{\varepsilon_l}{\varepsilon_a}$, where ε_l and ε_a are the axial and lateral strains, respectively. In this article an external uniform axial compression is applied but the method has been shown to be applicable for cardiac applications with internally applied stress as well, e.g. Langeland et al. (2003), Langeland et al. (2002).

To increase the accuracy of the lateral displacement estimates Konofagou and Ophir (1998) proposed to interpolate the RF-signals in the lateral direction. This way it is possible to obtain subpitch motion estimation. An axial one-dimensional kernel is chosen in the reference frame and correlated with a one-dimensional kernel in the interpolated comparison frame in a two-dimensional search region. The peak of the correlation function provides both axial and lateral motion.

The technique proposed is an iterative method with three main steps:

- The post-compression RF A-lines are globally stretched axially to compensate for the applied axial strain and an axial elastogram is generated. A weighted interpolation is performed in the lateral direction to create more A-lines and tissue motion is tracked laterally and a lateral elastogram is generated.

- The tracked segments are shifted to their assumed pre-compression state by the amount of estimated lateral displacement and new corrected post-compression RF A-lines are constructed. This step is performed to recorrelate of the signal due to the decorrelation caused by lateral motion. A new axial elastogram is generated and this step is repeated until the correlation coefficient of the axial elastogram is sufficiently high.

- The lateral elastogram is divided by the axial elastogram to generate a Poisson's ratio elastogram.

2.5.3 Beam-steered ultrasound imaging

Hansen et al. (2010); Techavipoo et al. (2004); Hansen et al. (2009) have suggested a solution to the lack-of-phase problem in the lateral direction using angular insonifications. Ultrasound RF signal are acquired from pre- and post-compression images at a various number of different angles thus containing the phase information in all directions.

The ultrasound data acquired at angles $\neq 0^\circ$ is stored in a rectangular grid, while it contains sample points acquired at an angle. This causes the image to be a skewed representation of reality. To reshape the data, the RF-lines are shifted by a certain number of points defined by *shift*, compared to the next RF-line

$$shift = \frac{D_x \sin \alpha}{D_y}, \tag{2.30}$$

where D_y is the axial resolution. A spline interpolation is performed because "shift" is usually not an integer. Interpolation is carried out in 1D instead of 2D to preserve RF phase information.

The displacement vectors were found with a 2D cross-correlation algorithm using a coarse-to-fine method (Lopata et al. (2009)).

Chapter 3

Methods

A two dimensional speckle tracking method was selected as the displacement map generator for this project; the method is presented in section 2.4.3. The reason for the choice was that the method is well documented in the literature, it has a long tradition and several useful applications. Thus it seemed like a good option, both because of the documentation and because of the relatively simple implementation.

The strain was estimated using the central difference theorem, presented in section 2.3.

The implementation of the speckle tracking algorithm and the strain estimation algorithm is explained in section 3.1.1 and 3.1.2.

A program was developed around the speckle tracking algorithm to keep track of all the calculated values and different functions needed to display the estimates. From this a graphical user interface (GUI) was created as a means of investigating the different parameters and their effects on the displacement and strain estimates. The GUI also allows for the image-series to be viewed as a cineloop. The structure of the program is presented in section 3.1.3. An explanation of the GUI and its functions is presented in section 3.2.

The developed program was implemented using MATLAB (The MathWorks Inc., Natick, MA, USA), version 8.2.0.29 (R2013b).

The implemented method was tested on simulated ultrasound images as well as ultrasound images acquired of and elasticity phantom. The data acquisition is presented in section 3.3.

3.1 Implementation

3.1.1 Normalized correlation search

The speckle tracking algorithm is built around a built-in MATLAB function (*Normxcorr2*). The input to the function is two arrays: the kernel and the search region. The function

performs a full search for the kernel within the search region; the kernel is placed over an equally sized area and a correlation coefficient is calculated by equation 2.28. Every possible configuration within the search region is tested, see figure 3.1. The return from the function is an array the size of the search region of correlation coefficients.

The largest value of the correlation coefficient array indicates the new position of the kernel in the subsequent frame. The location is defined by two coordinates, the axial and the lateral displacement estimates.

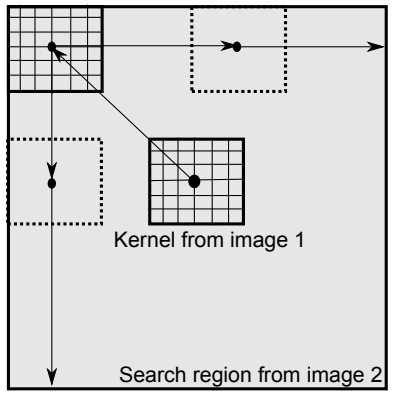

Figure 3.1: This is an example of how the built-in MATLAB function (normxcorr2, section 3.1.1) searches for the best fit of a kernel in a search region. The search starts by placing the kernel in the top left corner of the search region. A correlation coefficient, ρ, is calculated, and then the kernel is translated one sample to the right. This is repeated until the kernel is at the end of the search region. The kernel is then placed back on the left side but one sample down. The search is over when all possible configurations have been compared.

Interpolation

The movement of scatterers is not confined to discrete values but is a continuous function and thus interpolation is required to detect subsample displacement estimates.

Interpolation is a method for generating new samples in between two existing samples to get a finer resolution in between them (up sampling).

The interpolation is performed by a built-in function in MATLAB (*interp1*). The input to the function is the values and coordinates of the values that are to be up sampled as well as a new vector of coordinates. The new vector is created from the old coordinates but with several sub coordinates. The number of sub coordinates is the number of interpolated values the function will generate. A *spline* interpolation is used. A spline is mathematically defined as a smooth polynomial function that is piecewise defined.

Interpolation is performed on the correlation matrix (if the peak correlation coefficient is below 0.99) in an attempt to generate a correlation coefficient even closer to 1 at a subsample location. The values used for interpolation are the two neighboring points of the correlation peak. The interpolation is one dimensional and thus performed in one direction

at a time. The largest correlation coefficient from both interpolations is chosen as the new correlation coefficient for the displacement search and the new locations are used as the displacement estimates.

The algorithm has three adjustable parameters:

- Kernel size: the axial and lateral size of the kernel is defined by l depth samples and k A-lines. The size of the kernel defines the two-dimensional array used to estimate the displacment.
- Maximum lag: the axial and lateral maximum lags, i, j respectively, define the maximum number of samples the function will search for the kernel within. If the displacement is in fact larger than the maximum lags, the algorithm is sure to give a faulty estimate.
- Interpolation: the interpolation parameters decide how many new samples are created in between two old samples. The number of new samples can be different for the axial and lateral direction.

The kernel size and the maximum lag are both user defined sizes, as will be seen in section 3.2, but the interpolation is set within the program.

To estimate the displacement matrix for the entire ultrasound image, the image needs to be divided into several overlapping kernels and the displacement estimated for each kernel. Meaning the procedure presented above needs to be repeated for each kernel.

A function was developed to estimate the displacement of an ultrasound image (The code for the algorithm is found in appendix A, section A.1.1.) The inputs to this function is a two-dimensional matrix containing two subsequent RF-frames, an array of center points and the parameters presented above.

The array of center points is used to define the centers of the overlapping kernels and thus the search regions in the subsequent frame. The center points can be every sample in the RF-frames, but there is also the option to estimate the displacement for only a selected amount of samples, say every fifth sample or line instead, either axially or laterally. Thus a fourth speckle tracking parameter is introduced, the step size *s*. *s* is user defined as will be seen in section 3.2. Increasing *s* reduces the resolution of the displacement frame, but significantly reduces computation time as will be seen in section 4.2.4.

The output of the speckle tracking function is three matrices; the axial displacement matrix, the lateral displacement matrix and the correlation coefficient matrix.

3.1.2 Strain estimation

The strain is estimated using the central difference theorem, see equations 2.17 and 2.18. The strain estimation algorithm has two adjustable parameters:

- ΔAx: the number of samples to be used for the axial strain estimation.
- ΔLat: the number of lines to be used for the lateral strain estimation.

The strain parameters define the initial length of the segment that the strain will be investigated for, the parameter L_0 in equation 2.11.

If the step size, *s*, is set to be larger than 1, the length of the segment is the strain parameter (either axial or lateral number of samples) multiplicated with the distance between two points, $\Delta Ax * (stepsize_{axial})$.

ΔL of equation 2.11 is the displacement estimate of the end point of a segment closest to the transducer subtracted from the displacement estimate of the end point of the segment located the furthest away from the transducer.

The strain image is generated from the displacement matrix using convolution. A built-in function in MATLAB, *conv2*, takes a displacement matrix and a vector as input, as well as a shape specifier which determines the size of the convolved output matrix. The vector is a row of zeroes except for the endpoints which contain $\pm(1/\Delta Ax * stepsize_{axial})$ or $\pm(1/\Delta Lat * stepsize_{latal})$.

The code used for strain estimation is found in appendix A, section A.2.1.

3.1.3 Structure of program

Figure 3.2 illustrates the structure of the program created for the speckle tracking method. The program is linked to a graphical user interface, presented in section 3.2. The chain of events when the program is opened is like this: a file is loaded into the program (either a $.rf$ file from an ultrasound scanner, or a $.mat$ file from MATLAB). The files contain some information about the imaging parameters in addition to the RF-data. All parameters as well as the RF-data is stored in an object of a class, *ImageSystem*.

If axial or lateral displacement is chosen form the list of figures in the GUI (3.2), the program halts until a region of interest is defined in the B-mode image. An illustration of the region of interest defined in the B-mode image is found in 3.2.

Depending on the parameters set in the GUI (kernel size, search region, step size) the program calculates an array of center points within the region of interest, again see figure 3.2 step 1. The displacement of each point is calculated one at a time. The kernel is defined around each point in the template image and the search region is defined around the same point in the subsequent frame. After that each search is performed as described in the previous section, section 3.1.

The displacement estimates generated from the search are stored in two separate matrices, see figure 3.2 step 2.

Axial and lateral strain is calculated from the axial and lateral displacement maps, respectively. A strain map is generated by convolution of the displacement map with a one-dimensional segment of the length specified by the strain parameters as explained above.

In figure 3.2 (step 3) the strain parameters, ΔAx and ΔLat, are set to be two samples long, which means that the program estimates the strain of a segment three estimated points long. The estimated axial and lateral strains are stored in two different matrices as the displacement estimates.

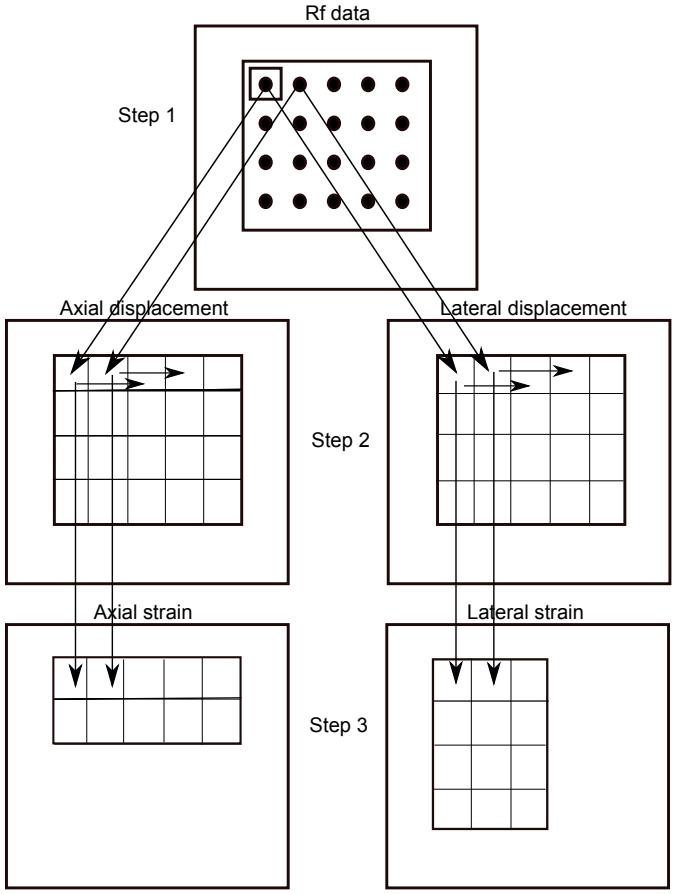

Figure 3.2: The structure of the program developed is represented by three steps. The program is linked to a GUI (figure 3.2, section 3.2), thus the GUI is the interface, while this program is running in the background. A B-mode image is always displayed as a default setting when a file is loaded into the program. Provided that either of the electable figures have been chosen, the chain of events is like this; Step 1: a region of interest is defined by the user, and within this region an array of center points is calculated based on the speckle tracking parameters (kernel size, maximum lag and step size) defined by the user. Step 2: The axial and lateral displacement is estimated for each point (see section 3.1.1 for a description of the searching procedure) The estimates are then stored in two different matrices. Also stored, but not shown in this figure, is a matrix of correlation coefficients. Step 3: (If a strain figure has been elected) The axial and lateral strain is estimated from the displacement matrices and stored in separate matrices. The length of the segment used for estimation is defined by the user. It is worth noting that the strain parameter set in the GUI is not the length of the segment in samples, but the number of displacement points used, see section 3.1.2. In the figure, both strain parameters (axial and lateral) are set to two points.

3.1.4 Representation of displacement and strain values in color images

Børstad (2010) implemented a function that would deal with "*the dynamic range of the strain values being time varying*" (Børstad (2010)), which means that colors change a lot through an image series of varying strain magnitude. Thus for a more pleasant visualization and easier interpretation of the strain image series, the values are thresholded and normalized.

The normalization is added to make it simpler to fit the estimated values to a color bar. When the estimates have a range form 0 to 1 the color range is produced by multiplying the normalized estimates with the desired color bar range. The scaling and normalization was based on statistical image processing, and a full description is found in Børstad (2010).

3.2 Graphical User Interface

A graphical user interface (GUI) was developed in order to be able to change displacement and strain estimation parameters in a simple way and display the results as a cineloop. The GUI was developed using the GUI created by Børstad (2011) as a model and an inspiration, though it was modified and adapted to fit the requirements and needs for the speckle tracking algorithm.

An image of the GUI is shown in figure 3.2. It has several functions that are useful for parameter optimization. An explanation of the different features and functions follows below:

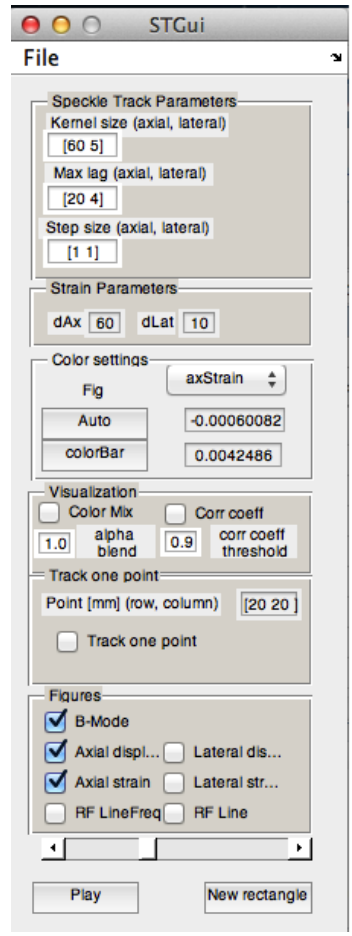

Figure 3.3: The GUI created to display displacement and strain values as videos.

- Speckle tracking parameters: The settings kernel size, max lag and step size controls the parameters of the speckle tracking algorithm explained in section 2.4.3 and above in section 3.1. The kernel size is specified as the number of samples and lines (lateral) used for the kernel in the axial and lateral direction. The final size of the kernel is $samples_{axial} * lines_{lateral}$. The maximum lags are also defined in number of samples and lines. The values do not specify the size of the search region, but the size that is added to the kernel size. The final search region in the axial direction is the addition of the axial kernel size and the axial maximum lag. The step size is defines the number of samples within the region of interest that will be used to generate the displacement matrix.

- Strain parameters: Strain parameters define the number of tracked points that will be used as the segment length for the strain estimation, as explained in section 3.1. *dAx* is the number of samples for the axial strain segment, *dLat* is the number of lines for the lateral strain segment.

- Color settings: Controls the presentation of the images. The max and min limits of the color bar can be manually decided by the user or automatically decided by pushing *Auto*. If *colorBar* is pushed, a color bar that shows the mapping between colors and values is produced.

- Visualization: The strain and displacement images can be shown with the B-mode image as a background by activating the color mix button. The window below de-

cides the alpha blend of the images. The blend is specified by the value in the window below. A lower value makes the overlaying image more see through and the structures in the B-mode image more visible. The checkbox for "CorrCoeff" is a choice to only display the estimates with a correlation coefficient equal to or larger than the value specified in the window below. The visualization settings as well as the color settings were implemented from an idea by Børstad (2011).

- "Track one point": If the button is clicked the program tracks and plots the point indexed in the window above through the whole image series. The first frame will then be used as the reference frame and the values set for the speckle tracking will be used as parameters for the tracking.
- Figures: A B-mode image is always shown as a default when a file is loaded into the program. Axial and lateral displacement and strain images are shown in separate windows. An RF A-line and the frequency of the line can be plotted. Which RF A-line is pre-defined by the program.
- Slider and play button: The slider can be dragged to iterate back and forth through the image series. The play button displays all the images in the series from the current point of the slider to the end of the file. All the currently open windows are played through.

3.2.1 Example of use

Figure showing the windows when program is in use. The figure is not meant as a result, just an illustration of the different options of figures and what the program looks like when in use.

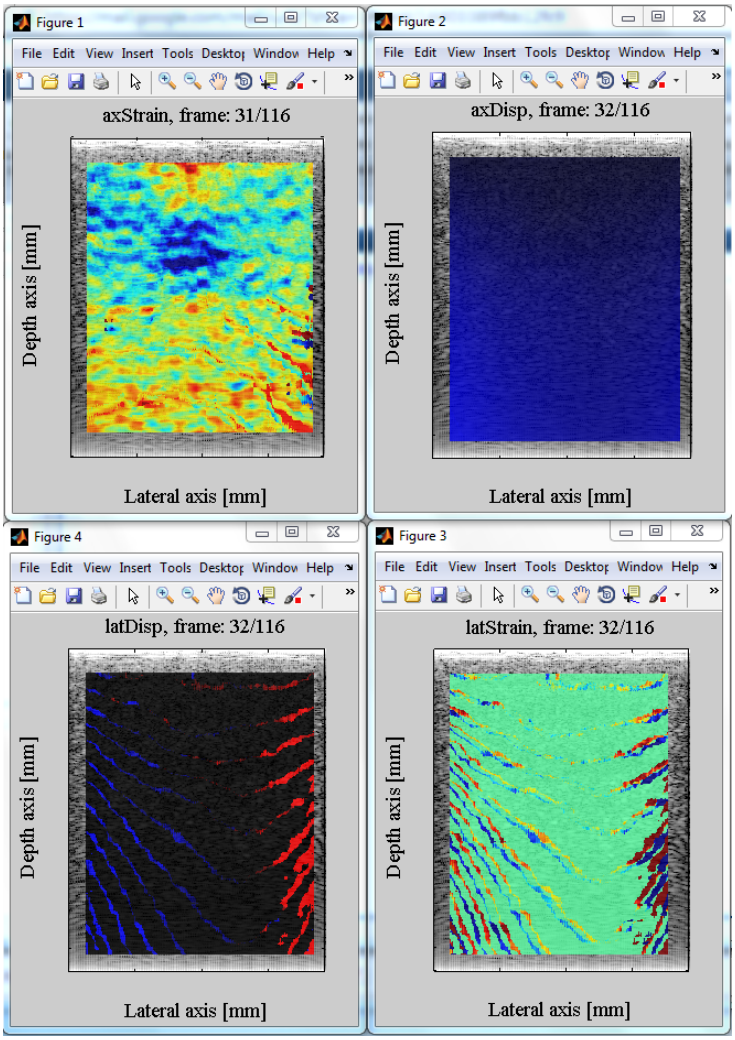

Figure 3.4: An example of what the program looks like when some of the possible figures have been elected, see figure 3.2. The electable figures are shown in separate windows. Top left displays the axial strain image, top right is the axial displacement image. At the bottom left is the lateral displacement image and the bottom right shows the lateral strain image.

3.3 Data acquisition

Simulated data and acquired elasticity phantom data were used to evaluate the performance of the speckle tracking algorithm created using MATLAB. Ultrasound images were simulated using the MATLAB based simulation program Field II. Ultrasound images of an elasticity phantom were acquired with the SonixMDP scanner provided by SINTEF.

3.3.1 Simulated data

To verify the ability of the developed speckle tracking method to detect axial and lateral displacement several data sets were simulated using Field II. The induced movement in the tissue was of known magnitudes making it simple to verify if the algorithm estimated the correct displacement values.

The scatterers were displaced in either axial or lateral direction. No deformation in the image was simulated to ensure that the pattern remained constant from frame to frame.

Field II

Field II is a MATLAB based program developed by Professor Jørgen Arendt Jensen. Used for this thesis is version 3.22 released on the 27th of October, 2013, and was downloaded free of charge from the Field II website http://field-ii.dk.

Field II is an acoustic field simulation program based on a method developed by Tupholme and Stephanishen (Tupholme (1969), Stepanishen (1971a), Stepanishen (1971b)). The approach relies on linear systems theory to find the ultrasound field through the spatial impulse response (Jensen and Svendsen (1992)).

The program calculates the convolution of the transmit excitation function (sine wave with a Gaussian envelope) with the spatial impulse response of the transducer. The spatial impulse response represents the emitted ultrasound field at a specific point in space as a function of time.

The transducer array is divided into small squares to enable the simulation of different transducer geometries. The response of the transducer is a summed response of all the squares.

The program requires the user to define the type of transducer to use (linear, curved, etc), the scanning sequence and the object to be imaged (a matrix containing the coordinates of the scatter points as well as their amplitudes). The coordinates are defined with respect to the transducer surface.

Simulation

As the first step of the simulation, the imaging system was put together from the functions provided by Field II. To make the simulated image system resemble the actual system used for neuronavigation, the parameters of the simulated system were set approximately the same as the parameters for Ultrasonix MDP scanner in nerve block mode (table B.2).

The transducer simulated was a linear transducer with 128 physical elements and center frequency (f_c) 10MHz. A Hanning window was used to calculate the apodization (explained in section 2.1.1) and 16 elements were used as the active aperture for each beam. The impulse response was modeled as a sine function depending on the sampling frequency, f_s, and the center frequency, f_0, of the transducer.

The sample frequency was chosen to be 100MHz because it is recommended by the creators of Field II. The transmit focus was set to be in the middle of the image in the axial direction with dynamic focusing for reception of the signals. Imaging is performed line-by-line from left to right in the image.

The second step of the simulation is to simulate a phantom. The phantom must be sent to the Field II functions as a matrix with *Nx3* rows and columns, respectively. *N* is the number of scatter points in the phantom and three is the number of dimensions (x, y, z) or (axial, lateral, elevational). The matrix of coordinates makes it easy to give the scatter points a new position in the image and thereby simulate a displacement of the scatterers as illustrated in figure 3.5. The black sphere in the image has been displaced 5mm laterally and 10mm axially.

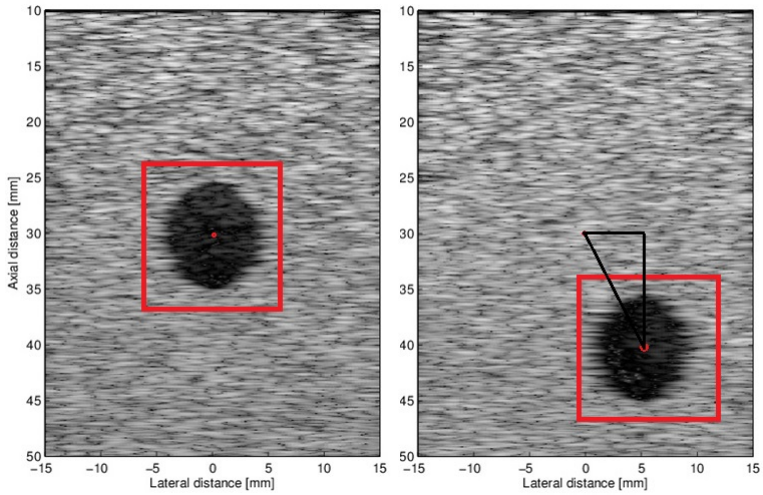

Figure 3.5: The coordinates and amplitudes of the scatterers are user defined and sent to the Field II functions as a three-dimensional matrix (coordinates) and one row-vector (amplitudes), as explained in section 3.3.1. Thus to simulate a movement in the image, the coordinates of the scatterers are simply changed, while the amplitudes are kept the same. This is an example of a B-mode image with a large black inclusion created with the imaging parameters listed in table B.2. The inclusion has been displaced 5mm laterally and 10mm axially, while the background of the image has been kept still.

Simulated data-sets for testing the method

Images with sine shaped displacement curves will be simulated to imitate the natural pulsation of the arteries in the brain. The parameters of the different data-sets are listed in table B.3 and B.5 in section 4.1.1 and 4.1.3, respectively.

Three data sets will be simulated to test the accuracy of the tracking algorithm:

- **Data-set 1:** is a time-series simulated with a varying axial displacement throughout the image. The sine amplitude was increased over eight regions in the image, from the bottom of the image with the largest amplitude ($\pm$ 1mm) to the top of the image with the smallest amplitude ($\pm$ 0.3mm). The data-set consists of 11 simulated images and the sine curve has a period of $T = 10$ images.
- **Data-set 2:** is a time-series with an induced uniform lateral sine displacement of amplitude ($\pm$ 1mm). It consists of 41 images with a uniform lateral displacement in the shape of a sine curve with a period, $T = 20$ images. Thus whole image series is of $T = 2$ periods.
- **Data-set 3:** is a time-series of 11 images of a varying lateral displacement. The amplitude of the sine curves was increased laterally over six regions in the image. Starting from the right hand side with a maximum amplitude of $\pm$ 2mm, and ending on the left hand side with a minimum amplitude of $\pm$ 0.3mm. The period of the sine curve is $T = 10$ images.

A sinus movement of the tissue is the expected motion of the brain tissue when the displacement is caused by the pulsation of arteries, which follows the heart cycle. A displacement of maximum $\pm$1mm is a realistic amplitude. The images in data set one and three allowed for the calculation of relative strain in the image as well, due to the varying amount of displacement in the image. In data set two the displacement is uniform and the relative stain should therefore be zero.

The first image in the data set was used as the reference image throughout the displacement estimation to illustrate the characteristic sine shape of the displacement curve.

Axial and lateral strain curves will be estimated for data-sets 1 and 3 using the central difference theorem presented in section 2.3.

Limits of speckle tracking method

To test the lower limit of the algorithm in the axial direction 14 images will be simulated with decreasing axial sine displacement. The amplitudes of the sine curves will be ranging from $\pm$ 0.1 mm to $\pm$ 0.0001 in mm, which corresponds to $\pm$ 13 to $\pm$ 0.013 in samples.

3.3.2 Ultrasound scanner

The scanner used is a 2011 SonixMDP (Ultrasonix, Canada) commercial scanner. The MDP system has the possibility of choosing research mode. This mode allows the user to

specify most of the parameters of throughout the ultrasound signal chain. When in research mode it is also possible to record and export radio-frequency (RF) data for post-processing on a personal computer.

It is possible to choose from different imaging modes on the scanner. The parameters, such as transmit frequency and frames per second, are predefined to fit the area of the body that is to be imaged. For this project Nerve block mode was used to test the method on the most realistic situation. The parameters for the nerve block mode are listed in table B.2 except for the sample frequency, f_s which is 38MHz for the Nerve block mode.

3.3.3 Elasticity phantom

Ultrasound images of an elasticity phantom were acquired as a second way of testing the implemented method. The elasticity phantom has a known stiffness distribution and it is therefore possible to verify if the results are correct or not. The phantom is from CIRS (Norfolk, VA, USA) and is an Elasticity QA Phantom (Model 049).

The elasticity phantom contains several inclusions that are *isoechoic* (same reflection property) but of different Young's modulus (stiffness property) as the surrounding material. Thus the inclusions are supposed to be impossible to detect in the B-mode images but made visible with strain processing.

Images were acquired while the phantom was manually pushed down with the transducer probe by the author. One cycle of compressing the phantom and letting up was kept close to one second, to imitate the cycle of the heart and the natural pulsation of the arteries in the brain.

The phantom was only compressed from the top in the axial direction as the phantom was confined in a box on all other sides. The results from imaging the elasticity phantom are displayed in section 4.2.

Two image-series will be acquired using the compression method explained above, the first of a harder inclusion than the background, the second of a softer inclusion than the background. The images will then be used to investigate the effects of changing the displacement and strain parameters (presented in sections 3.1.1 and 3.1.2, respectively) on the resulting images.

The reason for the parameter testing is that optimizing the parameters for the speckle tracking needs to be performed for every single data-set investigated, because the optimal parameter configuration changes depending on the size of the movement in the data-set. The tests that will be performed are:

- A very small kernel size.
- A very large kernel size.
- A very small search region.
- A very large search region.
- Various step sizes in the axial direction.

The test of reducing the step size will only be performed in the axial direction due to the already poor resolution in the lateral direction.

A table of the properties (Young's modulus, speed of sound, etc.) are found in B.1 in appendix B.

Chapter 4

Results

The chapter is divided in two parts. The first section contains the results obtained from the simulated images. The second section contains results acquired from the elasticity phantom.

4.1 Simulated data

4.1.1 Axial displacement

Data set 1 - varying axial displacement

Figure 4.2 shows the expected and the estimated movement of the scatter points simulated for data-set 1. The tracked points are displayed in the simulated ultrasound image in figure 4.1. Table B.3 shows a list of the coordinates of the points as well as the simulated displacement in both mm and samples.

In figure 4.2, the expected movement is shown as lines while the estimated movement is displayed as star markers. The displacement estimates are well fitted to the expected movement and no outliers are observed for this data-set.

Figure 4.3 shows the strain curves calculated from the displacement estimates.

- The leftmost figure shows the strain calculated from a segment of three tracked points. The table B.3 shows that the segments point 1 to point 3 and point 2 to point 4 both have a difference in displacement (Δl) between the extremities equal to 0.4mm. The segments point 3 to 5, point 4 to 6, point 5 to 7 and point 6 to 8 have a difference in displacement between the extremities of the segments equal to 0.2mm. The last segment point 7 to 9 has an initial negative difference in displacement due to the zero movement in point 9. The figure shows three strain curves which is expected. The first two segments will only be separated by the small difference in initial length (L_0) between them. The middle segments have equal displacement

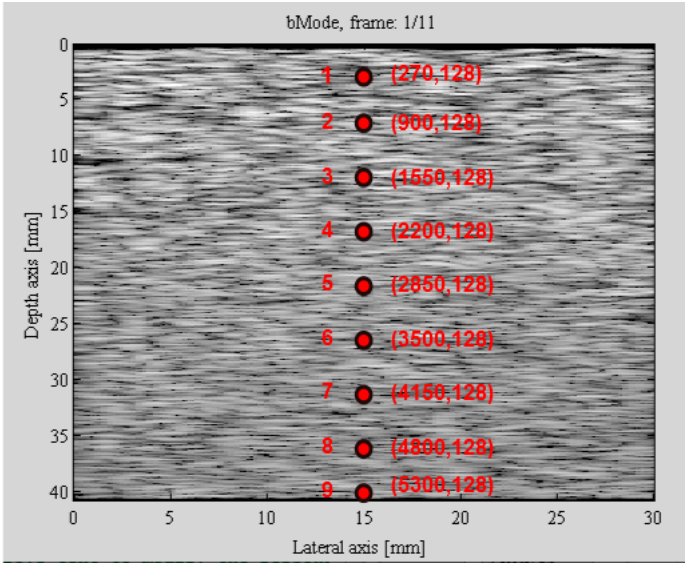

Figure 4.1: The red circles in the B-mode image indicate the positions of the points tracked in figure 4.2. The amplitudes of the displacement sine curves for the points are listed in table B.3.

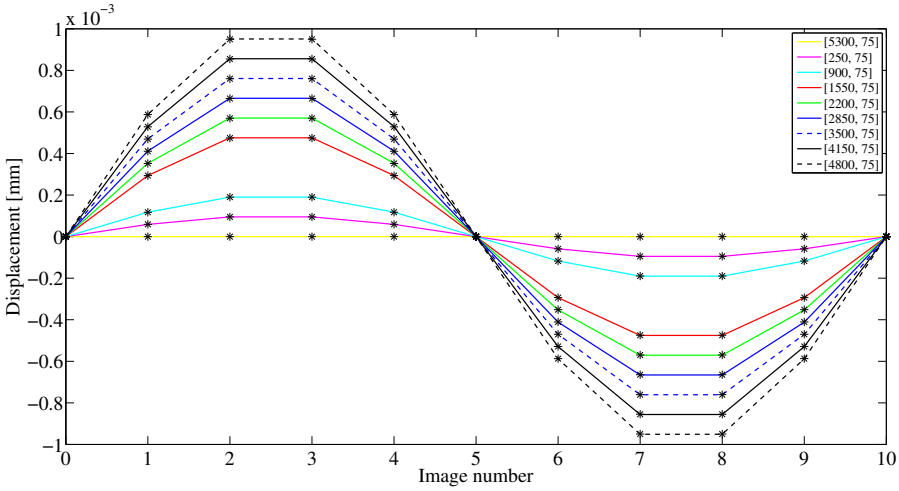

Figure 4.2: The expected axial displacements of the points defined in figure 4.1 are displayed as full or dotted lines. The estimated axial displacement values are displayed as the black star markers which follow the expected displacement. The exact numbers of the displacement amplitudes are listed in table B.3.

and equal distance between them. The last segment shows an opposite strain pattern which is correct.

- The middle figure shows the strain curves calculated from a segment of four tracked points.
- The rightmost figure shows the strain curves calculated from a segment of five tracked points.

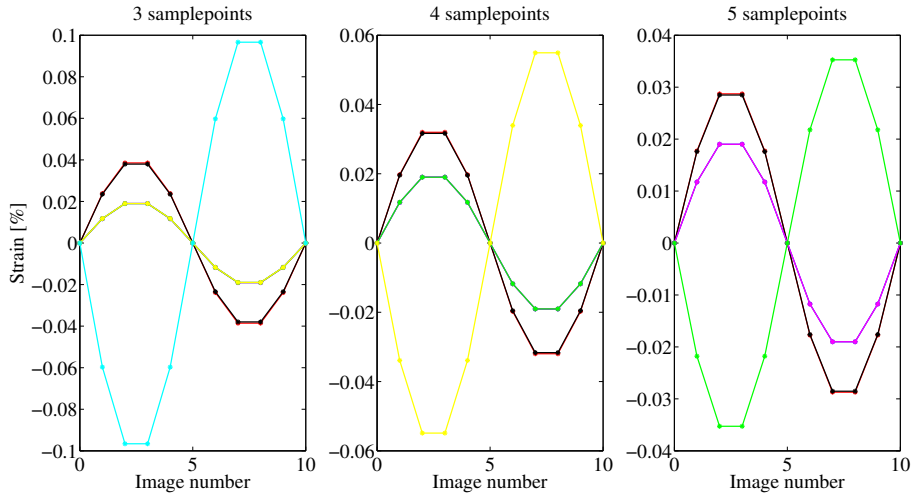

Figure 4.3: The axial strain curves were estimated from the displacement estimates in figure 4.2. The leftmost figure shows the strain estimated using a segment length of three displacement points, the middle figure shows the strain estimated using a segment length of four points and rightmost figure shows the strain estimated using a segment length of five points. Note that the number of points is not the length of the segment in samples, see section 3.1.2

Interpolation- with and without Figure 4.4 shows half a period of two displacement estimates from data-set 1. The blue star markers display the interpolated displacement estimates, the red markers display the estimates without interpolation. It is clear from the figure the blue markers are slightly closer to the expected movement. However the estimates without interpolation show a high accuracy as well.

4.1.2 Axial limit of speckle tracking method

Figure 4.5 shows the algorithms ability to detect sub-mm and sub-sample displacement in the axial direction. The curve is put together by one period of 14 displacement curves of decreasing sine amplitude. The amplitudes of the curves are displayed in table B.4 in appendix B.

Figure 4.6 is a zoomed view of figure 4.5. The figure shows where the estimates started to somewhat diverge from the expected movement, although the errors are very small. The method shows the first start of breaking down for curve 14 with displacement amplitude

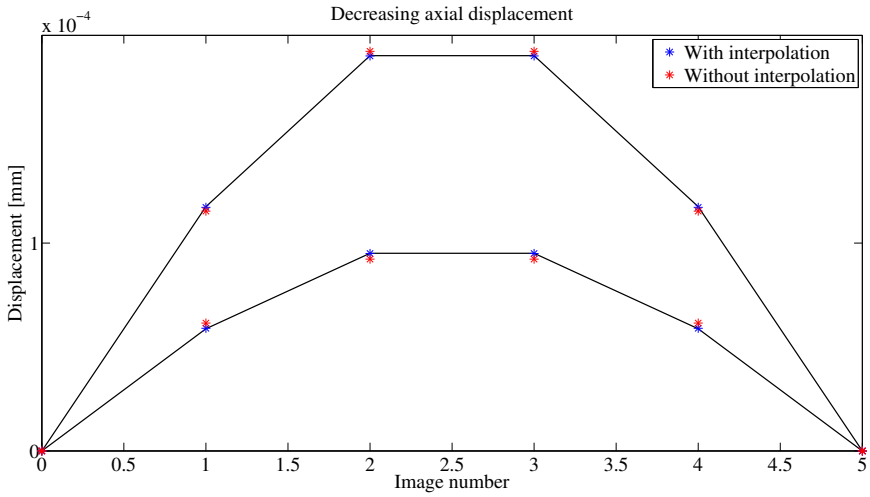

Figure 4.4: The axial displacement estimates were interpolated using spline interpolation (see section 3.1.1). The interpolated values are displayed as blue star markers, while the red star markers display the non-interpolated values. The full black line shows the expected displacement. It is possible to observe that the interpolated estimates are slightly better placed on the expected movement line, but the difference is nearly insignificant. Thus for the simulated images, the method performs well without interpolation, still all the searches were in general performed with interpolation.

0.0013 samples (see table B.4). For this displacement the algorithm detected zero displacement.

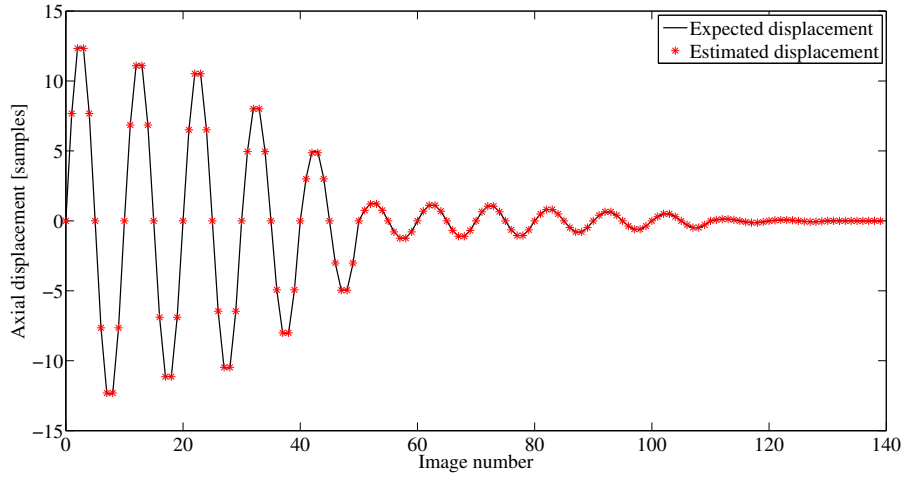

Figure 4.5: Expected and estimated axial displacement from $\pm$ 13 samples to $\pm$ 0.013 samples were simulated to observe when the method was no longer able to detect the correct displacement. The red star markers display the estimated displacement, the black full line the expected displacement. For this figure, the markers are observed to fit the expectation perfectly, but it is difficult to see if that really is the case for the smallest displacement estimates. The amplitudes of the displacement curves are listed in table B.4.

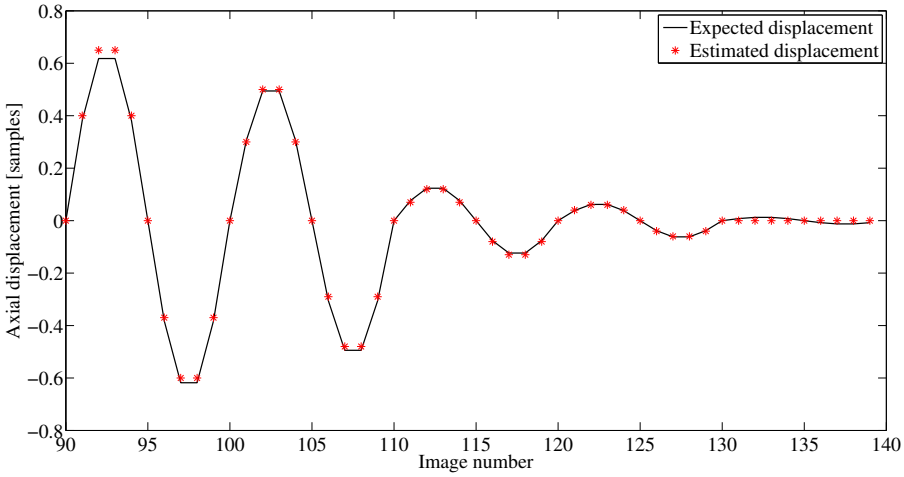

Figure 4.6: To better observe the subsample displacement estimation a zoomed in view of figure 4.5 is presented. The expected shows expected and estimated axial displacement ranged from $\pm$ 0.13 samples to $\pm$ 0.013 samples. It is possible to observe that after image 130, the algorithm has not been able to detect any movement. It is possible that the limit observed here could be solved with an even finer interpolation.

4.1.3 Lateral displacement

Data set 2 - uniform lateral displacement

Figure 4.7 shows the expected and estimated displacement of an image with simulated compression of a uniform lateral sine wave with amplitude ± 1mm at two different positions. The figure shows two examples of tracked points.

The estimates of the lateral displacement show a tendency of a sine curve, but the correlation coefficients of the estimates are below 0.9 which makes the estimate unreliable. The inaccuracy of the estimates seems to be correlated with the decrease of the correlation coefficient. When the lateral displacement increases, the correlation coefficient decreases. Some axial movement was also detected, even though there was no simulated axial displacement for this data set.

Figure 4.7 shows the expected and estimated lateral and axial displacements as well as the correlation coefficients.

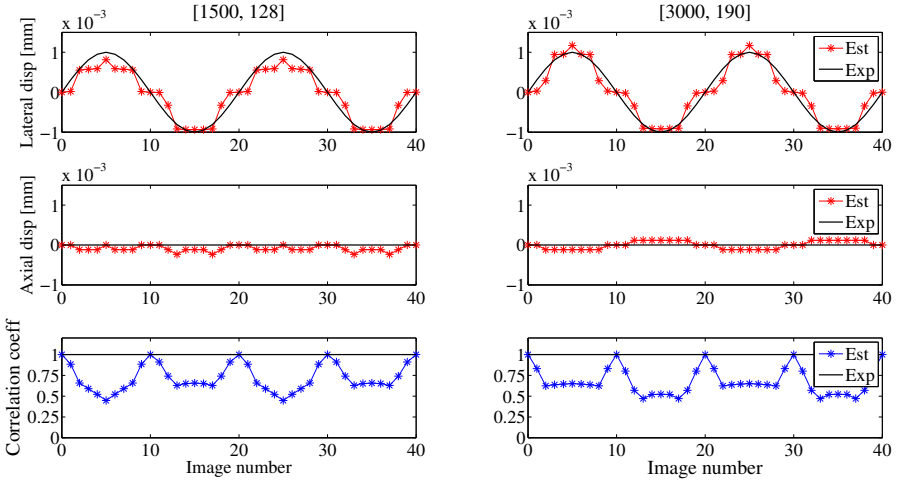

Figure 4.7: The expected lateral displacement of the simulated phantom (in mm) when subjected to force from the right hand side. The lateral and axial displacement as well as the correlation coefficient of the search is displayed for two different locations in the simulated image. The tracking is of poor quality, seeing as the lateral estimates do not fit the expected displacement particularly well, the axial displacement curves are non-zero and the correlation values fall below 0.9 as the displacement increases. It is observed that for every time the speckle pattern returns to its initial position, the algorithm is able to track the correct displacement.

Data set 3 - varying lateral displacement

Figure 4.9 shows the expected and estimated displacement of data-set 3. The coordinates of the points that were tracked as well as the amplitudes of the sine curves are shown in table B.5. The locations of the points are illustrated in 4.8.

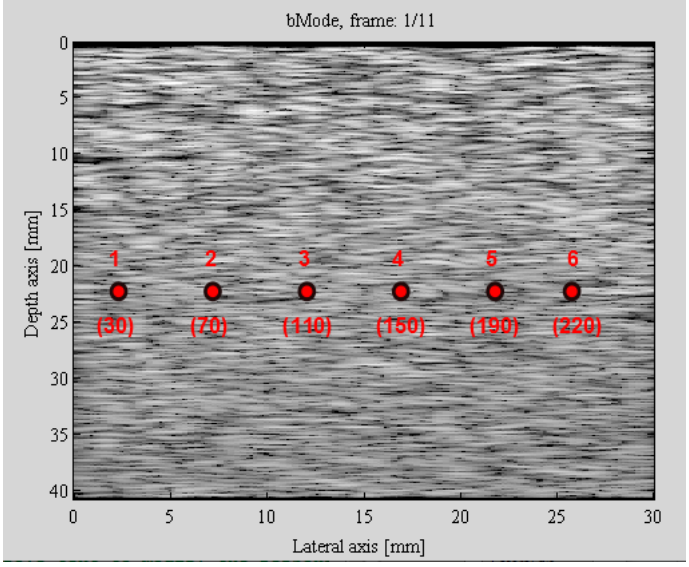

Figure 4.8: The red circles in the B-mode image indicate the positions of the points tracked in figure 4.9. The amplitudes of the displacement sine curves for the points are listed in table B.5.

Figure 4.9 shows the same tracking inaccuracy as for data-set 2. The leftmost regions in the image were displaced with the largest amplitude. The tracked points from these regions show a slightly better correlation with the expected movement. The rightmost regions were displaced less and show nearly zero displacement through the whole image series. The estimated axial displacement as well as the correlation coefficients for the tracked points are shown in figure 4.10.

No displacement in the axial direction was simulated for this image series. The correlation coefficients are seen to decrease in the same way as for data-set 2. As the lateral displacement increases, the correlation coefficients decrease.

The lateral strain curves calculated from the lateral displacement maps are shown in figure 4.11. The curves are calculated for segments of 3 points, 4 points and 5 points. The lateral strain curves were expected to follow the sine shape. The strain curves in figure 4.11 are calculated from the estimated displacement, thus the strain curves are incorrect as a consequence of the incorrect displacement estimates.

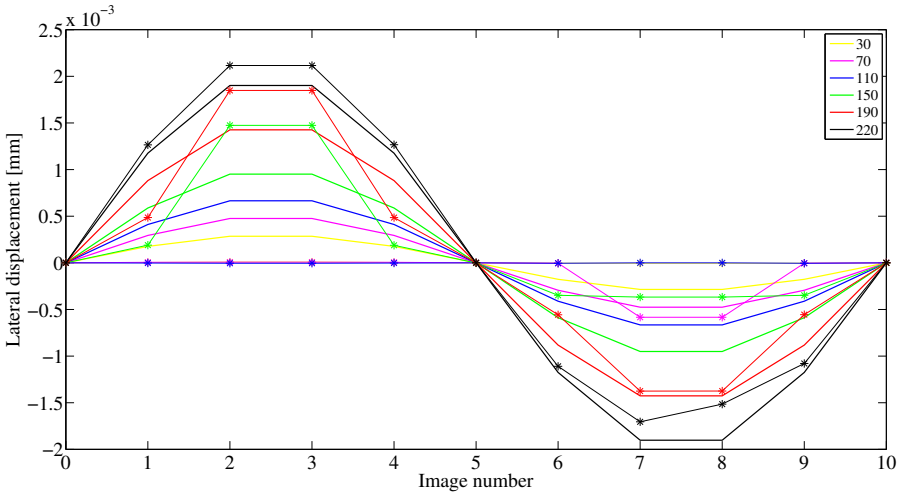

Figure 4.9: The expected lateral displacements of the points defined in figure 4.9 are displayed as full or dotted lines. The estimated axial displacement values are displayed as the star markers of the same color as the expected displacement line. The exact numbers of the displacement amplitudes are listed in table B.3. The displacement estimates do not particularly well follow the expected curves. It is observed that only the three leftmost tracked points show any movement, the rest are estimated to be zero.

Alternative verification of lateral displacement estimation

Due to the poor accuracy of the lateral tracking, an alternative method of displacing the RF-data was performed as a second attempt of verification of the method.

To simulate a sine displacement in the tissue 12 images were created by adding rows of zeros to each side of one simulated image manually. A number of rows from 1 to 5 were added in turn to create the displacement. The result of the tracking is shown in figure 4.12.

The estimated displacement shows a perfect match with the expected displacement.

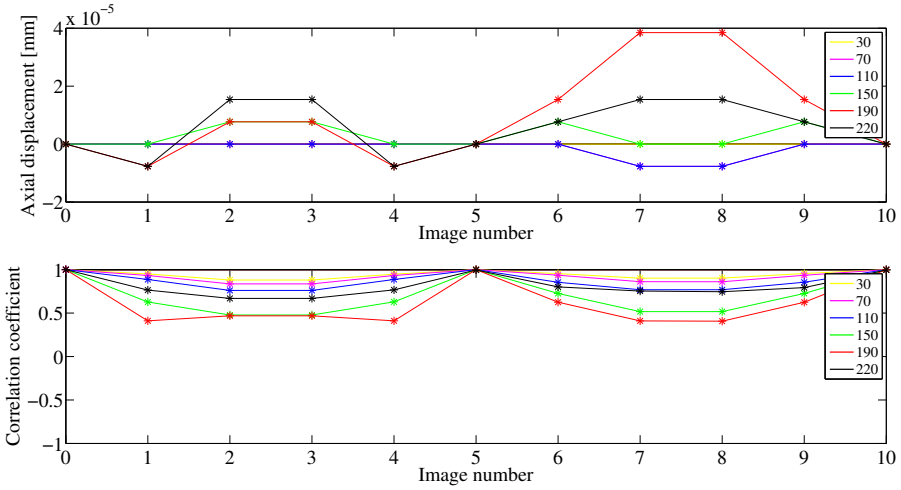

Figure 4.10: The estimated axial displacement (upper plot) and correlation coefficient (lower plot) of the estimation in data set 3. Non-zero axial displacement was estimated for data-set even though the simulated movement was purely lateral. The correlation coefficients of the searches display the same shape as in figure 4.7. The coefficients decrease with increasing amplitudes, and increase when the scatteres return to their initial position.

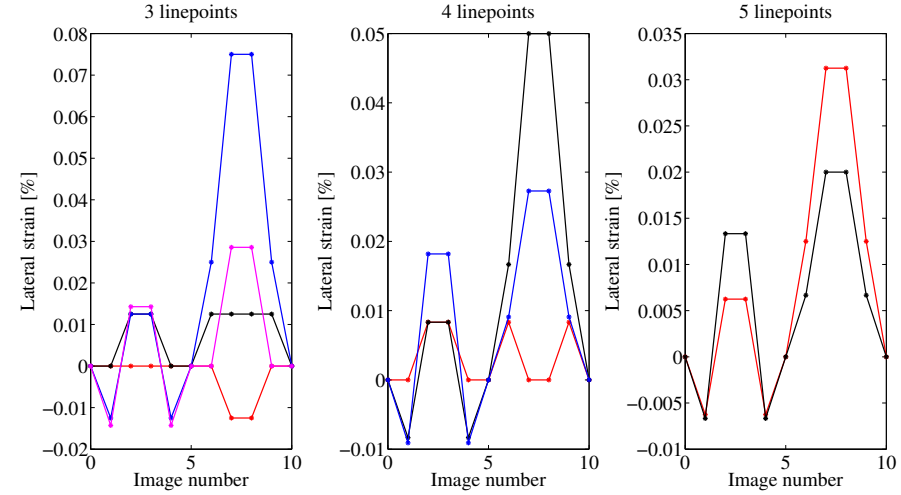

Figure 4.11: The lateral strain curves estimated from the displacement estimates of figure 4.9, are observed to be of wrong shapes and values as a consequence of the faulty displacement estimates. The leftmost figure shows the strain estimated using three samples as the segment length, the middle figure is calculated using a segment length of four points and the segment length in rightmost figure was five points long. Note that the number of points is not the length of the segment in samples, see section 3.1.2

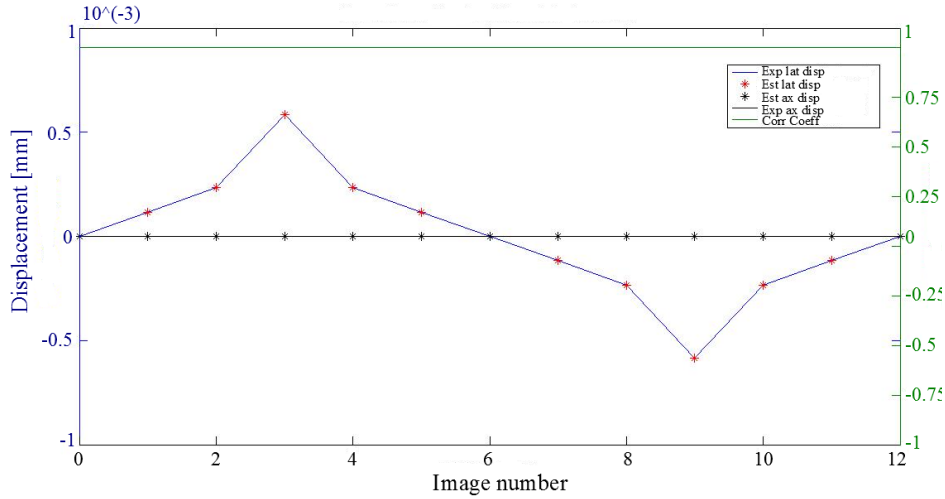

Figure 4.12: The lateral tracking was decided to be tested in an alternative way due to the faulty estimates of the previous lateral displacement figures (4.9 and 4.7). Instead of simulating the lateral displacement, one image was used and displaced manually by adding columns of zeroes to the sides in turn. This way the speckle pattern was sure to remain constant. The movement was made with the intention of imitating a sine movement. The displacement estimates are observed to fit the expected movement perfectly, with correlation coefficients of one and zero axial displacement.

4.2 Phantom

Images of an elasticity phantom with inclusions of varying Young's modules were acquired to test the algorithm. The phantom was compressed with freehand palpation as described in section 3.3.3. The parameters of the displacement and strain estimation are listed in table B.6. Some of the estimated displacement and strain images of the elasticity phantom are displayed with the B-mode image as a background. This is how the images could be displayed on a real ultrasound scanner.

4.2.1 Hard inclusion

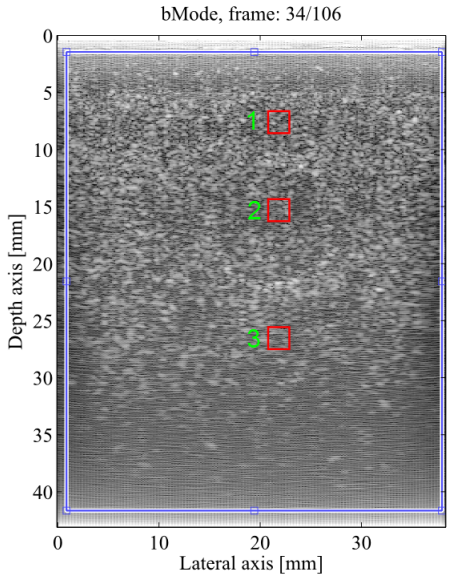

Figure 4.13: The B-mode image is an image chosen at random from an image-series of an elasticity phantom compressed and decompressed periodically using freehand palpation. It contains a barely visible hard inclusion. The inclusion is *isoechoic* with the surrounding material and is therefore not visible in the B-mode image,however the inclusion has a different stiffness property (Young's modulus). Three regions are marked in red, where the middle region is the location of the hard inclusion. The displacement and strain through the image series is plotted in figure 4.16 (axial) and 4.17 (lateral).

Figure 4.13 shows a B-mode image of a hard inclusion. The inclusion is barely visible in the B-mode image but is made visible with strain imaging. Three regions are marked in the B-mode image. The first region is above the hard the inclusion, the second region is within the hard inclusion and the third region is below the inclusion. The axial and lateral displacement and strain curves of these regions through the acquired image series is shown in figure 4.16 and 4.17, respectively.

Figure 4.14 shows a displacement matrix as well as a strain image of the hard inclusion. The frame is part of an image series and was chosen at random for display.

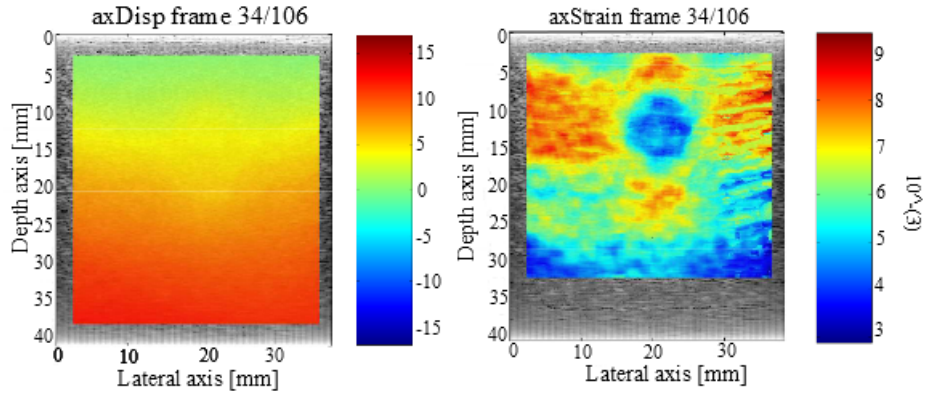

Figure 4.14: The axial displacement estimated of the hard inclusion is shown to the left in the figure. The frame number is the same as the B-mode frame shown in figure 4.13. The strain image (right hand side) was estimated from the displacement matrix and the hard inclusion was made visible in blue. The inclusion has a clear contrast from the surroundings. The strain image also shows a background that seems to be varying in stiffness, although the stiffness parameter of the background is uniform.

In the strain image the hard inclusion is clearly visible in blue in the middle of the image, but there are several other regions in the image where structures of different stiffnesses could be suspected to be located. From the description of the phantom, the stiffness of the background is supposed to be uniform.

Figure 4.15 shows the lateral displacement and strain estimated from the same image as figure 4.14. The displacement and strain estimates seem to be curving along a circular shape at the location of the hard inclusion. But only parts of the image seem to be moving while there are regions in between where the displacement is estimated to be zero. It is difficult to determine if the lateral strain estimates are due to actual lateral motion or just an effect of noise in the image.

Figure 4.16 shows the estimated axial strain and axial displacement of the regions marked in the B-mode image in figure 4.13. The curves show that the displacement is increasing with depth in the image. The strain curves show that there is less strain in region number 2 than in region number 1 and 3.

Figure 4.17 shows the lateral displacement and strain estimated from the marked regions in figure 4.13. The curves do not show a lot of movement in either of the regions. From the estimated strain, the curves show that the magnitudes of the strain values in region number 2 are smaller, but as there is practically no straining in region one it is difficult to compare the results in the lateral direction.

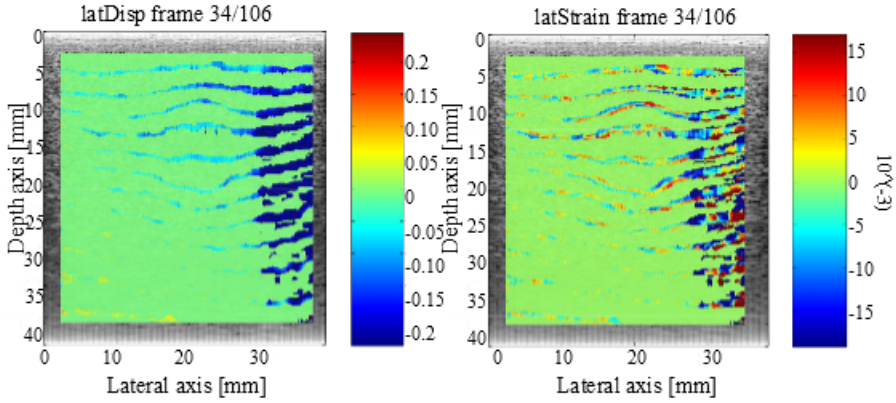

Figure 4.15: A lateral displacement image of the same frame as in figure 4.13 is displayed to the left, while the strain image estimated from the displacement matrix is shown to the right. The lateral displacement and strain is observed to be alternating between a small movement and zero movement throughout the image, which seems rather unnatural. At the location of the hard inclusion, the moving regions show signs of curving, but especially in the strain image it is difficult to interpret the color values to decide if that region strains less.

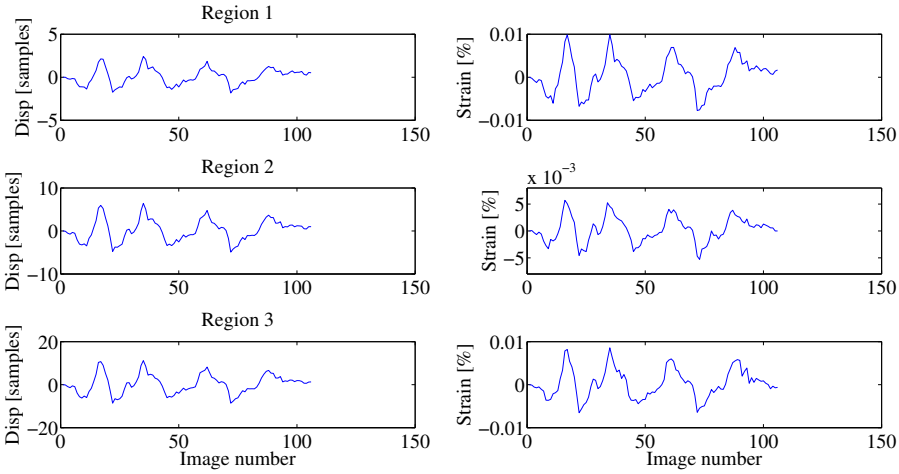

Figure 4.16: The axial strain and displacement was plotted from three selected regions of the hard inclusion through an image series. The regions are shown in image 4.13, but the plotted values are from the displacement and strain images 4.14. The curves are seen to displace and strain periodically as was the intention. Region 2 which is the region of the hard inclusion is observed to strain less than the surrounding regions.

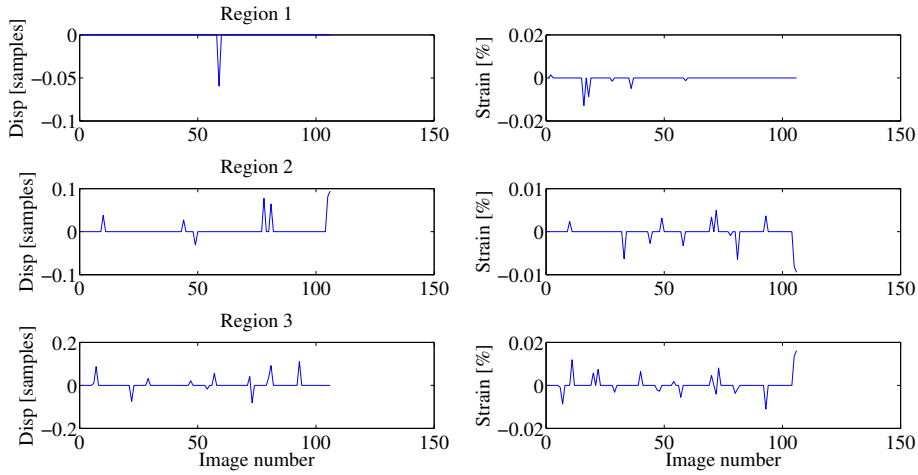

Figure 4.17: The lateral strain and displacement was plotted from three selected regions of the hard inclusion. The regions are shown in image 4.13, but the plotted values are from the displacement and strain images in4.15. The curves do not show a particular pattern and are therefore difficult to interpret and compare against each other. The curves seem to show more movement towards the deeper end of the image.

4.2.2 Soft inclusion

Figure 4.18 shows a B-mode image of an inclusion that is made of softer material than the background. The inclusion is practically impossible to visualize in the B-mode image. Three regions are marked in the image. They represent the same locations as the marked regions in figure 4.13. The plotted displacement and strain is displayed in figure 4.21 and 4.22.

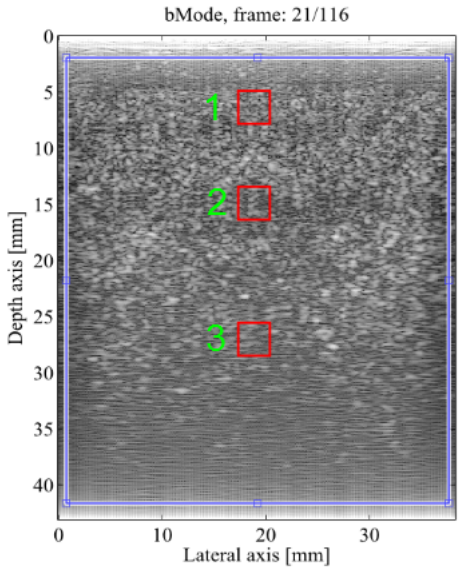

Figure 4.18: The B-mode image is an image chosen at random from an image-series of an elasticity phantom compressed and decompressed periodically using freehand palpation. It contains a barely visible soft inclusion. The inclusion is *isoechoic* with the surrounding material and is therefore not visible in the B-mode image,however the inclusion has a different stiffness property (Young's modulus). Three regions are marked in red, where the middle region is the location of the soft inclusion. The displacement and strain through the image series is plotted in figure 4.21 (axial) and 4.22 (lateral).

Figure 4.19 shows an axial displacement and strain image from an image series acquired of a soft inclusion. The displacement image to the left shows an increasing displacement towards the deeper end of the image. The strain image, to the right, shows an approximately circular region with a higher strain value than the surrounding material. This indicates that the soft inclusion has been made visible by strain imaging.

Figure 4.20 shows the estimated lateral displacement and strain for the same frame as figure 4.19. The displacement image (left) shows a displacement that is positive on the right side of the image, while it is negative on the left side of the image. This could indicate that there is a structure in located in the center of the image that is separating the directions of motion. As for 4.15, only narrow horizontal lines in the image seems to be

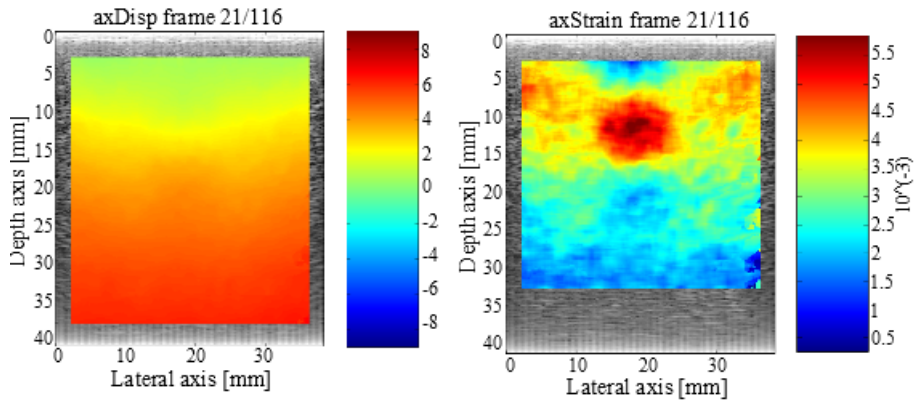

Figure 4.19: The axial displacement estimated of the soft inclusion is shown to the left in the figure. The frame number is the same as the B-mode frame shown in figure 4.18. The strain image (right hand side) was estimated from the displacement matrix and the soft inclusion was made visible in red. The inclusion has a clear contrast from the surroundings. The background of strain image is slightly more uniform in this image than the strain image in 4.14.

moving, while there are regions in between them that show zero displacement. The strain image (right) does not clearly show any indication. It is difficult to deduce any pattern from the image due to the noisy color values.

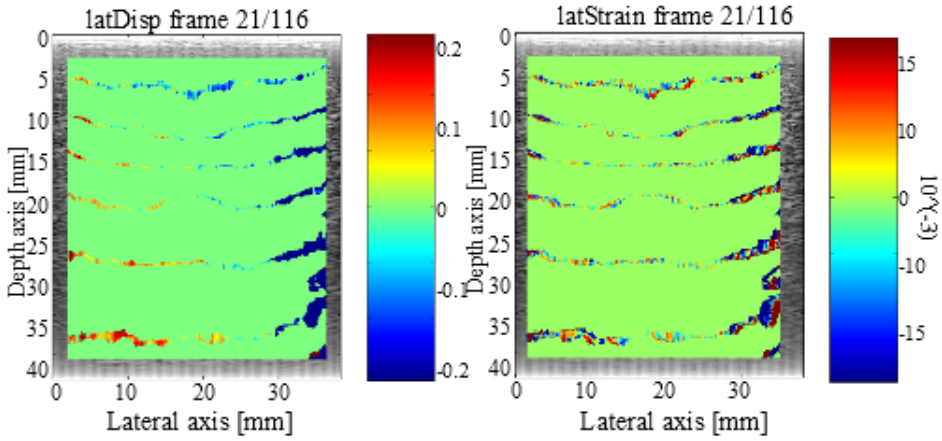

Figure 4.20: A lateral displacement image of the same frame as in figure 4.18 is displayed to the left, while the strain image estimated from the displacement matrix is shown to the right. The displacement image shows different color values to the left and to the right in the image, indicating that it is moving to separate sides, which could be an effect of the inclusion in the middle of the image, although the indication is vague. The lateral displacement and strain is observed to be alternating between a small movement and zero movement through the image, as for figure 4.15.

Figure 4.21 shows the axial displacement and strain estimated from the regions in

figure 4.18. The displacement increases with depth, as also seen in 4.16. The strain, however, is observed to be increasing in the middle region, while showing less strain in the surrounding regions, especially in the top region.

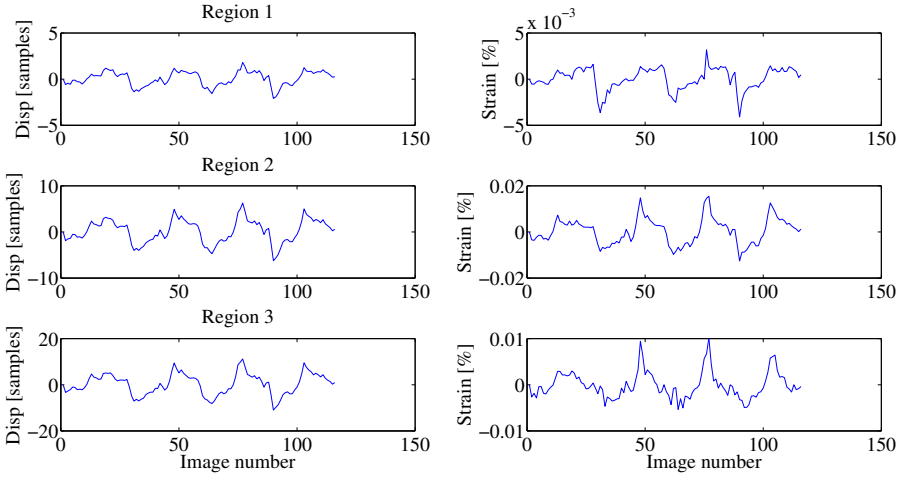

Figure 4.21: The axial strain and displacement was plotted from three selected regions of the soft inclusion through an image series. The regions are shown in image 4.18, but the plotted values are from the displacement and strain images 4.19. The curves are seen to displace and strain periodically as was the intention. Region 2 which is the region of the soft inclusion is observed to strain more than the surrounding regions, although the difference compare to the lower region is small.

Figure 4.22 shows the lateral displacement and strain curves estimated from the same regions. As for figure 4.17 the lateral displacement and strain does not seem to follow a particular pattern, and the strain for the displacement regions is difficult to interpret and compare.

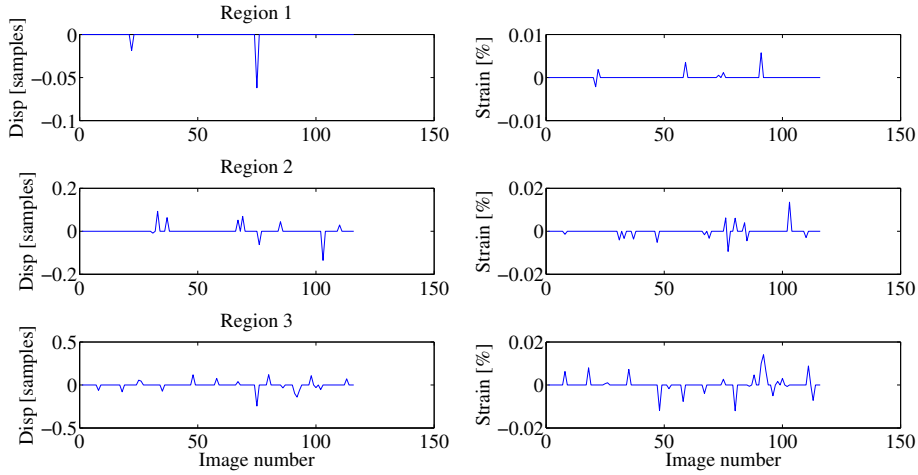

Figure 4.22: The lateral strain and displacement were plotted from three selected regions of the soft inclusion shown in image 4.18. The plotted values are from the displacement and strain images in 4.20. As for figure 4.15 it is difficult to interpret the curves. No clear pattern is observed, except for that the image seems to strain more in the deeper end of the image as seen in figure 4.15.

4.2.3 Correlation coefficient thresholding

A feature implemented on the GUI is the ability to remove the estimates of lower quality than a limit set by the user. Figure 4.23 shows a displacement and a strain image where the correlation threshold was set to 0.9. The estimates with a correlation lower than 0.9, are removed and the background image is displayed. The observed images only show a few areas of poorer correlation indicated by the pointing arrows. There is no obvious pattern in the placement of the regions of poor correlation, such as a very large movement.

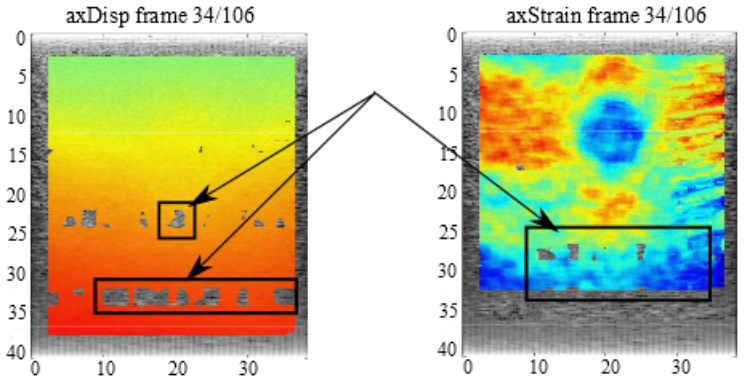

Figure 4.23: The axial displacement and strain image with correlation coefficient thresholding are observed to have small areas where the samples were to poorly correlated for display and are thus removed. From the images there is no apparent reason why the poor correlation occurred at those exact regions. They seem to be positioned randomly.

4.2.4 Varying speckle tracking parameters

This section shows the effects that varying the speckle tracking parameters has on the resulting displacement and strain images. The parameters are the kernel size, the maximum lag and the step size. A description of the parameters is presented in section 3.1.1. The displacement and strain images are displayed without the B-mode images as background.

Kernel size

The kernel size ([60 5]) used for the previous displacement and strain images of the soft inclusion (figures 4.19 and 4.20) was chosen because it was observed to give good results for the image-series investigated. This section is meant to illustrate the trade-off between accuracy and resolution for the kernel size described in section 2.4.3.

Figure 4.24 shows the axial and lateral displacement and strain images with a kernel size of [5 5] samples and lines, respectively. The images clearly show a much noisier estimates than the strain images of the soft inclusion in figures 4.19 and 4.20. The reduction of the kernel size looks to have decreased the ability of the method to track the correct displacement.

Figure 4.25 shows the effects of choosing a very large kernel size. The images (most noticeable in the axial strain image) seem to be smeared out, probably due to the loss of spatial resolution. The size of the estimated images is observed to be reduced compared to figure 4.24 as an effect of choosing a large kernel.

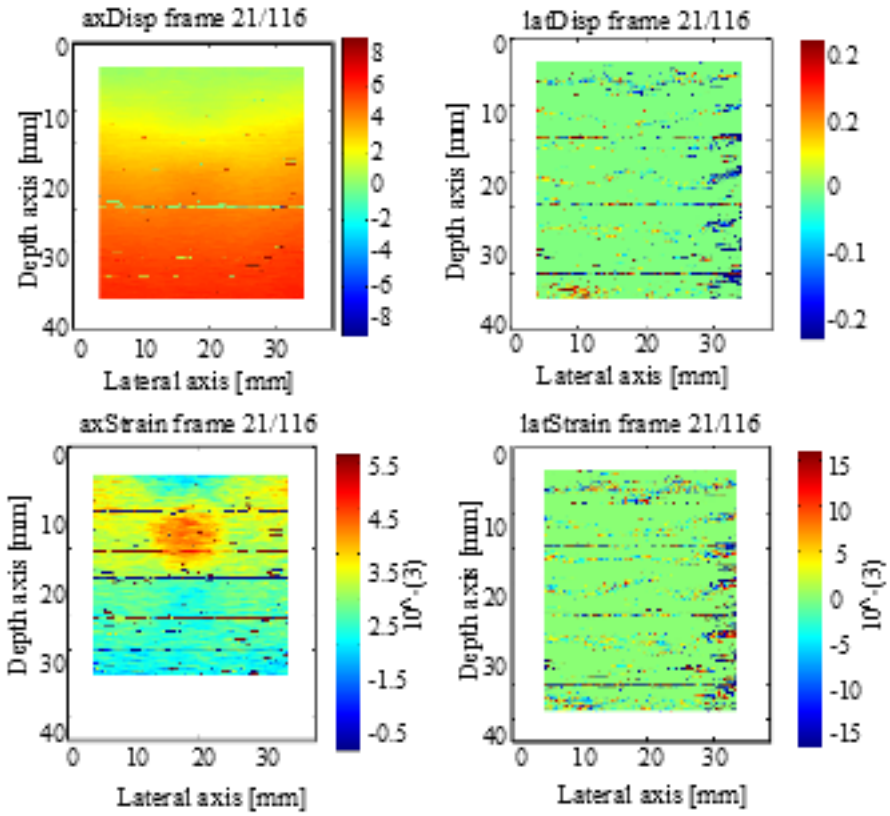

Figure 4.24: A correlation search was performed with a small kernel size [5 5], samples and lines, respectively. The images clearly show noisier estimates than the images of the soft inclusion in figures 4.19 and 4.20. The ability of the method to track the correct estimate depends on the uniqueness of the pattern defined by the kernel. The size used for this search was clearly too small.

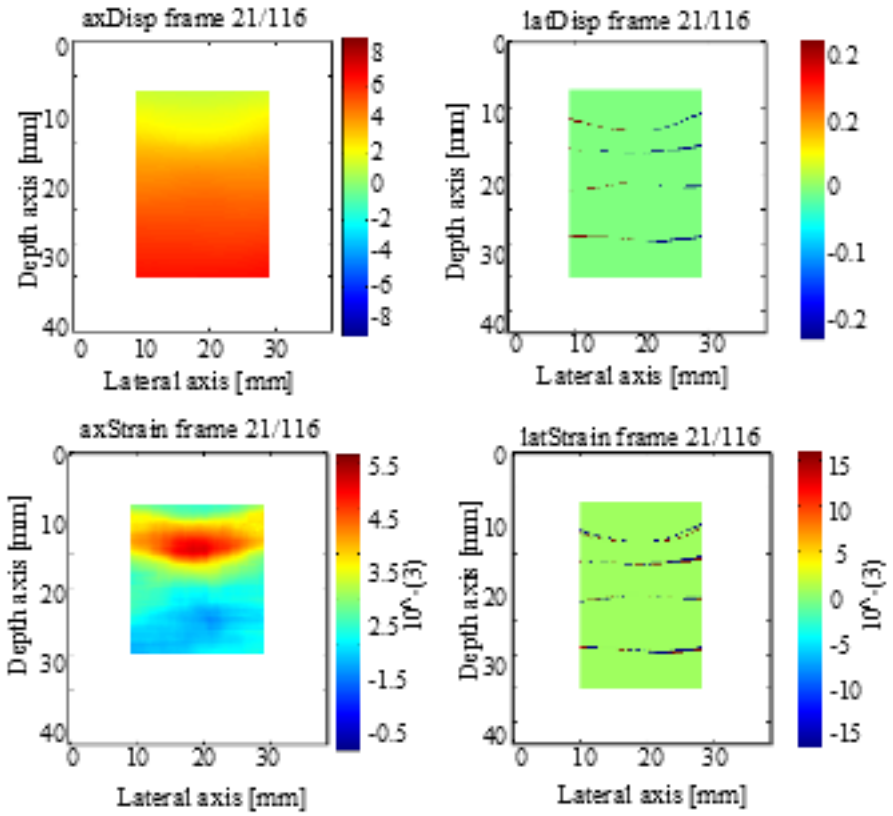

Figure 4.25: A correlation search was performed with a large kernel size [200 40], samples and lines, respectively. The images show less detail and seem to be smeared out compares to the images in figure 4.19. The large kernel reduces the resolution of the displacement and strain image by averaging the displacement over a larger array of samples.

Maximum lag

The maximum lag ([20 4]) chosen for the images in figures 4.19 and 4.20, was chosen because after testing, this was a size that seemed to include all of the displacement values observed.

Figure 4.26 shows the results of choosing a very small search region. The images were displayed with a correlation thresholding of 0.9, thus the estimates found were not of poor enough quality to be removed, but they were clearly not the correct estimates, compared to figure 4.19 and 4.20.

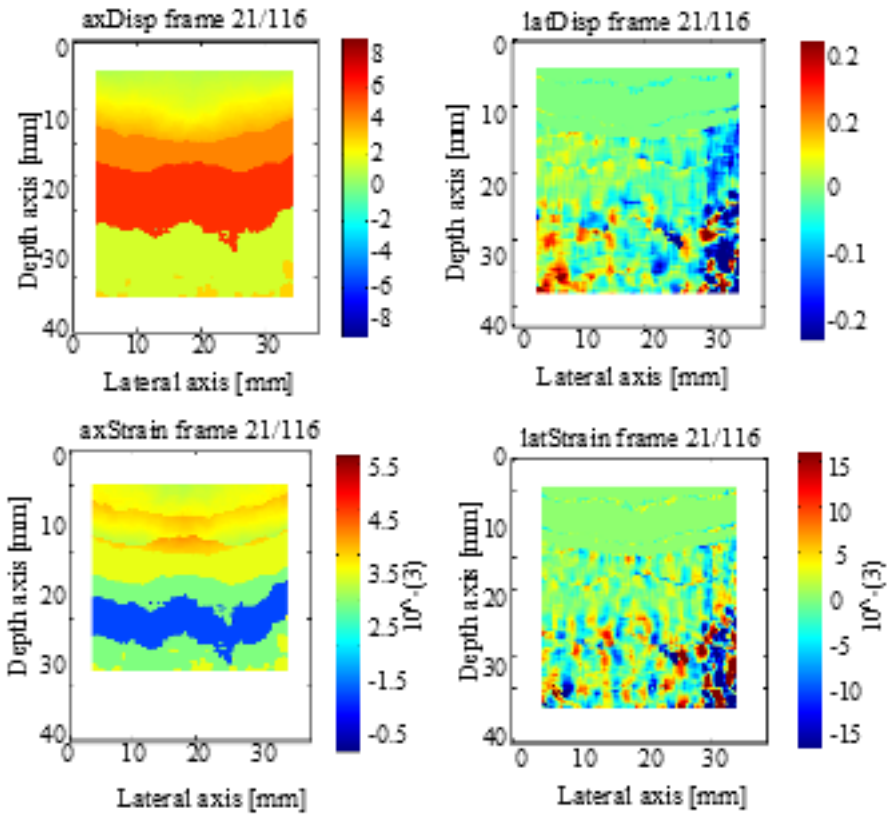

Figure 4.26: A correlation search is performed with a small search region: [4 2], samples and lines, respectively. The images are the result of the algorithm tracking the wrong displacement due to the limits of the search region. The images were displayed using correlation thresholding of 0.9. Therefore the estimates are not of poor quality, but still incorrect.

Figure 4.27 shows the effect of choosing a very large search region (size [100 40], samples and lines, respectively). Comparing the images to figures 4.19 and 4.20, the difference observed is not very large.

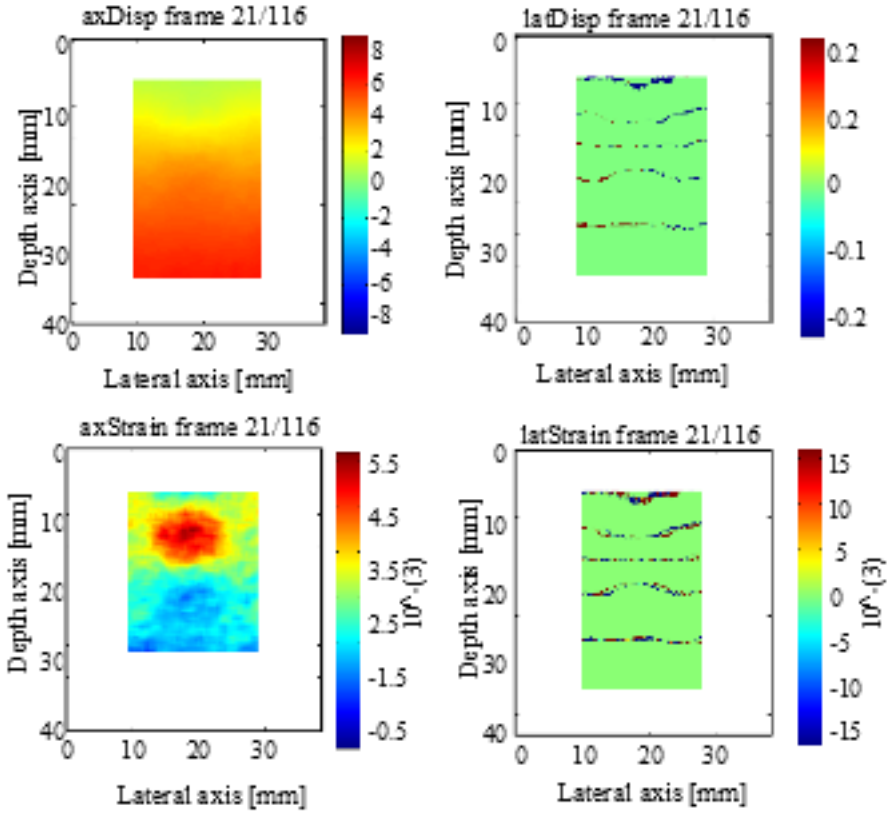

Figure 4.27: A correlation search was performed with a large search region: [100 40], samples and lines, respectively. The images do not show many incorrect estimates and are not so different from the images estimated in figures 4.19 and 4.20.

Step size

The step size decides how many displacement estimates are produced per frame. The test of reducing the step size was only performed in the axial direction due to the already poor resolution in the lateral direction.

The step size used for the images in the sections above was [5 1], samples and lines, respectively (see table B.6).

Figure 4.28 shows the effect of increasing the axial step size. The difference between the images acquired with a step size of one and a step size of five is negligible. Thus the decision was taken to estimate images with a step size of five (above) as it reduces the time of estimation considerably.

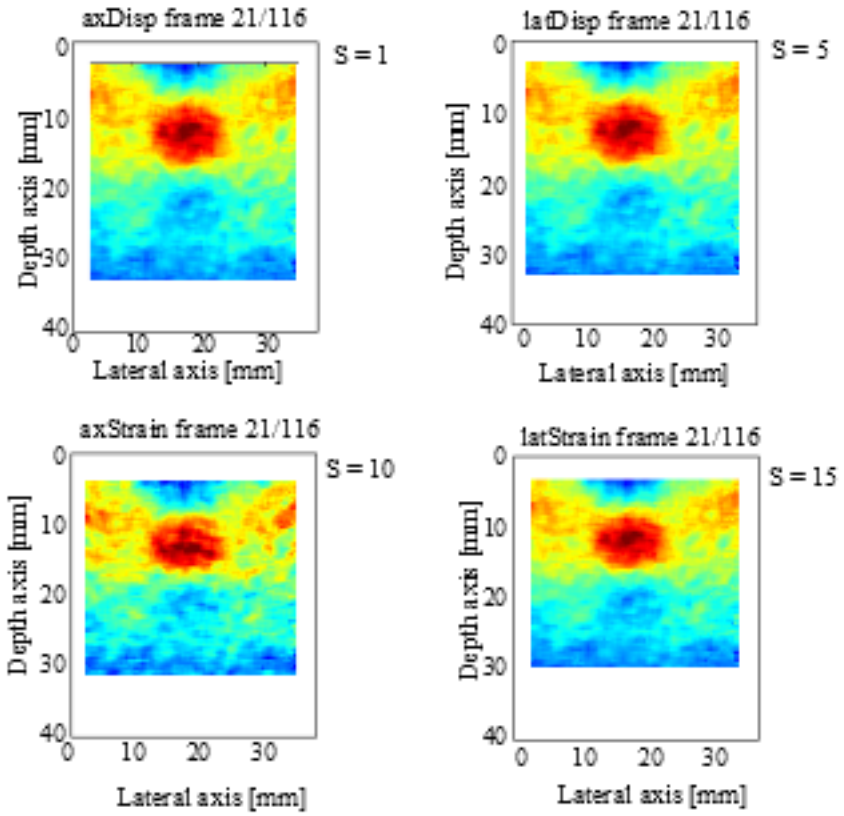

Figure 4.28: The speckle tracking performed with increasing axial step size, S is the step size in the figure. The images estimated with a step size of one and a step size of five are impossible to separate, therefore the decision was made to use an axial step size of five in all of the results presented above. The images estimated with a step size of 10 and 15 show a slight reduction in the size of the soft inclusion and were therefore discarded.

4.2.5 Varying strain parameters

Figures 4.29 and 4.30 shows the effects of varying the length of the estimation segments in the axial and the lateral direction, respectively.

Figure 4.29 shows that by varying the strain segment in the axial direction, the size of the inclusion changes slightly. The first image of the series, where *dAx* is equal to 5 samples, shows almost nothing but noise. As the length of the segment increases it is easier to observe the inclusion and the background becomes more uniform. The last image of the series, where *dAx* is equal to 110 samples shows an inclusion that has a reduced size. Thus increasing the length of ΔAx seems to give the strain estimates a better accuracy but a poorer spatial resolution.

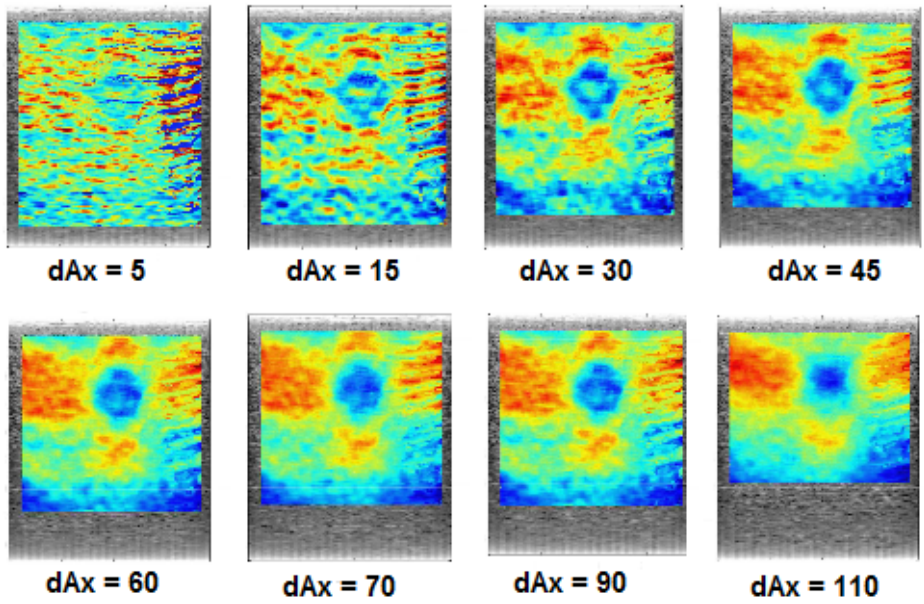

Figure 4.29: The effects of varying the length of the estimated strain segment in the axial direction are as observed from the figure that a longer segment produces a less noisy image; the inclusion is more visible and the background more uniform. The frame used to vary the axial segment length is the same strain frame as in figure 4.14, the color bar was therefore omitted from this figure.

The effects of changing the lateral segment length is shown in figure 4.30. The frame used is the same as the frame from figure 4.15. As commented before, it is difficult to draw any conclusions from the lateral strain images, but the effects seen of varying the length of the segment is in agreement with the findings above in figure 4.29. The estimates are less resolved and more uniform with increasing segment length.

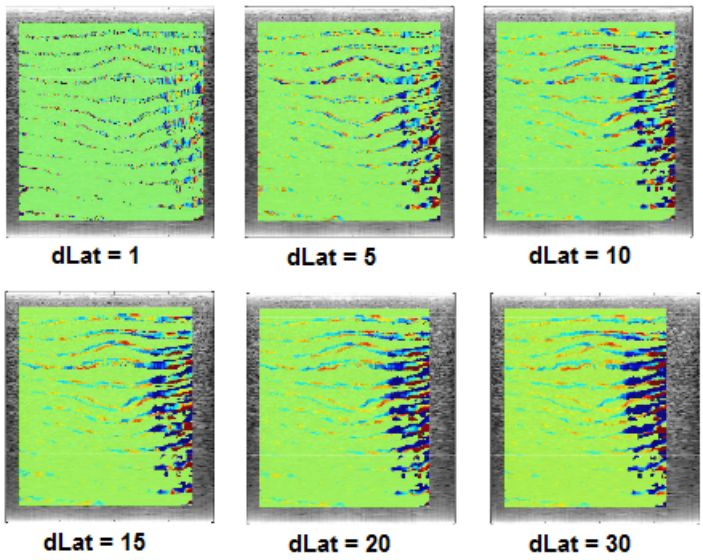

Figure 4.30: The effects of varying the length of the estimated strain segment in the lateral direction are the same as the effects of varying the length of the segment in the axial direction (figure 4.29). The images, though difficult to interpret, are observed to increase in uniformity with increasing segment length, as well as reduce in resolution. The frame used to vary the axial segment length is the same strain frame as in figure 4.15, the color bar was therefore omitted from this figure.

Chapter 5

Discussion

A discussion of the acquired results will be presented first. Following is a discussion of the different parameters and features that were important in changing the quality and appearance of the estimated displacement and strain images.

5.1 Displacement estimation

The performance of the algorithm will be discussed in the axial direction first, then the performance in the lateral direction.

5.1.1 Axial displacement estimation

Axial displacement estimation was first tested on simulated images with a known, purely axial displacement. The results (section 4.1.1 and 4.1.2) have shown that the method is capable of estimating the correct displacement, even when the motion is very small. Due to the spline interpolation used (see section 3.1.1), the algorithm can detect subsample displacements as small as 0.065 samples which is shown in figure 4.6. In the simulated image, neither lateral nor any elevational movement occurred, thus no signal decorrelation occurred. With no signal decorrelation, the method was expected to perform the tracking perfectly, as it did.

A limitation of the simulated images, or rather an advantage of the simulated images and a limitation of real data, is that the sample frequency used for the simulated images was 100MHz, because it was the recommended by the creators of Field II. At such a high sample frequency, the signal was very resolved and thereby very unique thus making it easier to track. The simulated images represented an absolutely ideal situation in the axial direction, thus it cannot be expected that the algorithm will perform with such a high precision for data acquired with an ultrasound scanner (of a lower sample frequency).

In the images acquired of the phantom, both lateral and elevational movement probably occurred in addition to axial movement. Axial displacement images of an elasticity phantom are shown in section 4.2 (figures 4.14 and 4.19, to the left). Nevertheless, the

images show no sign of faulty estimates, thus the algorithm seems to be performing well for phantom images as well, but it is difficult to determine for sure as the displacement was unknown and dependent on the stress induced by the manual palpation.

5.1.2 Lateral displacement estimation

The lateral tracking of the simulated images shown in section 4.1.2 and 4.1.3 were very inaccurate. There are two possible reasons for these results; either the algorithm was not able to track lateral displacements, or the pattern changed too much for the algorithm to recognize it.

We therefore decided to introduce an alternative displacement method (presented in section 4.1.3) where the pattern was sure to remain constant. The reasoning was that if the algorithm were to track the correct displacement in this situation, it would indicate that the problem lied with the simulated images. Seeing as the algorithm was able to track the correct displacements using this method, possible sources of error of the images are explored below.

Possible sources of error

The Field II simulation program required the user to define the imaging system. A possible source for error is the apodization we introduced to the active elements of the transducer. The apodization (explained in section 2.1.1) of the simulated transducer weights the transducer elements that are active during creation of a specific beam.

If the weighting is incorrect, the beam could be transmitting at an angle compared to the depth axis. This would change the appearance of the scatter points in the image and both the amplitudes of the scatterers and their position on the depth axis, thereby changing the speckle pattern. Even though this was not possible to observe when looking at the images, it is a possible source of error for the lateral displacement estimation. Due to the time limitation of this project, the exact error of the estimation will need to be a task for future work.

The lateral displacement tracking from the phantom images is shown to the left in figure 4.15 and 4.20. The lateral displacement images are definitively of poorer quality and more difficult to interpret than the axial displacement images. While they both show indications of movement, it seems unnatural that only certain regions of the phantom would move while the others in between remained completely still. The phantom was as mentioned in section 3.3.3 only compressed axially, and it is therefore not a particularly qualified test to determine the performance of lateral displacement.

With the rather strange appearance of the lateral displacement images, it is difficult to determine whether the observed estimates are the results of actual movement or just noise. Therefore further testing and especially a more qualified test is needed to determine the performance of the algorithm in the lateral direction.

5.1.3 Interpolation

Lateral tracking is, as explained in the theory more inaccurate than axial tracking due to the coarse resolution in the lateral direction (Righetti et al. (2003)). For this reason, in addition to the need for tracking subsample displacement, the correlation values have to be interpolated.

A possible error of the *spline* interpolation is that when several estimates fit the same peak correlation coefficient, the built-in interpolation function picks the estimate at the first position with this correlation value. Thus the interpolated correlation value may in some cases give a less accurate displacement estimate. This is a particular fault of the function used, therefore other methods for doing the interpolation could be looked into as well.

5.2 Strain estimation

Strain curves were calculated from the simulated displacement estimates as a verification of the central difference strain estimator presented in section 2.3 (equations 2.17 and 2.18). The axial curves (figure 4.2) displayed the strain as expected due to the accurate displacement estimates. The lateral strain curves did not display the expected strain as a consequence of faulty displacement estimates, which was expected as well.

As observed in figures 4.14 and 4.19, the developed method was able to estimate and display different areas of stiffness. The inclusions were clearly visible with a good contrast in the strain images, while practically invisible in the B-mode images. Although the inclusions were visible, the background of the images were relatively noisy and displayed what looked to be several structures of different stiffness, however the background of the phantom was supposed to be uniform in stiffness. The noise is either caused by the displacement estimates or by the strain estimator.

The strain was estimated by a central difference (CD) estimator as presented in section 2.3 in equation 2.17 and 2.18. This method only included the displacement estimates at the end points of the segment to estimate the strain. A possible improvement would be to use a more robust strain estimator.

A more robust strain estimator is the least squares strain estimator (LSQSE) described by Kallel and Ophir (1997). The LSQSE takes into account all displacement estimates of a segment. It was shown in the same article that the LSQSE improved the signal-to-noise ratio (SNR) for the strain compared to using the CD estimator. This was also confirmed by Børstad (2011). However, it is a slightly more computationally complex estimation. For the speckle tracking method, which is already very time consuming, it would need to be further considered if the LSQSE would be a good choice of estimator.

5.3 Parameters

A section of the results was dedicated to investigating the effects of the speckle tracking and strain parameters on the resulting images. A discussion about optimal settings will be discussed below.

5.3.1 The effects of varying speckle tracking parameters

Section 4.2.4 shows the effects of changing the kernel size. The kernel size is as mentioned before (section 2.4.3) a trade-off between resolution and robustness of the estimates. Choosing a very small kernel size was shown in the results to be insufficient for correct pattern recognition, and resulted in faulty estimates and noise in the image. Choosing a kernel size that was large noticeably reduced the resolution of the image and gave the image a smeared look.

Choosing the correct maximum lag is important because, as explained in section 2.4.3, if the displacements in the image are larger than the search region, the algorithm will give faulty estimates. As observed in section 4.2.4, the algorithm can estimate a movement with a high precision, but it can still be the wrong displacement vector. Thus, choosing the maximum lag is always a possible source of error. On the bright side, the results also showed that the effect of choosing a large search region was unnoticeable. Thus the maximum lags should be defined to be larger than the expected displacement rather than smaller.

An observed effect of choosing a very small axial maximum lag was that the lateral displacement image was estimated to have more movement than the regions observed in the other lateral displacement images, see figure 4.26.

The step size was the last parameter to be investigated. As mentioned in section 4.2.4, the effect of increasing the step size to five instead of one was not noticeable thus that setting was used for the displacement estimation for most of the results. It gave the advantage of reducing the computational time by five, which was welcomed when a full image took 4000 seconds to estimate.

The appearance of the lateral displacement images could look like they were a consequence of using an increased step size, but this has been tested and although not shown in the results, the lateral displacement images had a similar appearance for both estimation with step size one and five.

Even if it was not visible in the images for this project, the resolution was in fact reduced by five, and in a clinical setting where there might many targets of interest, not one inclusion, reducing the resolution is perhaps not such a good idea.

5.3.2 The effects of varying strain parameters

Figure 4.29 shows the effect of changing the length of the segment used for axial strain estimation. The strain estimates were observed to be more accurate for longer strain segments as was already expected from the findings in Børstad (2011). A more uniform appearance was definitively an advantage, seeing as the inclusion was barely visible in first image of figure 4.29, but the figure also shows is the reduction in spatial resolution which follows when increasing the segment length. As mentioned above, the spatial resolution was not an issue for this project when trying to visualize one inclusion, but in a clinical setting it might not be optimal.

Figure 4.30 shows the effects of increasing the segment length in the lateral direction.

Changing the length makes the color of the strain estimates slightly denser and more uniform, but the images are still difficult to interpret. Therefore before drawing a conclusion about the effects of the strain segment length in the lateral direction, more tests are needed.

It is difficult to decide upon any general rules for the optimal parameters. The optimal settings will be dependent upon the magnitude of movement of the particular images, the need for resolution and perhaps the uniformity in the image as well as the sample frequency with which the images were acquired.

5.4 Correlation thresholding

The correlation coefficient was used as a measure of quality of the estimates. It is a valuable tool for removing noisy regions in the image, and as a means of validating the parameter settings. Care must be taken though, it cannot be trusted blindly as was shown in figure 4.26 where the estimates had a high correlation coefficient but did not show the correct displacements.

Figure 4.23 shows the effects of removing estimates with a correlation coefficient below 0.9 on an axial displacement and strain image. A low correlation coefficient for a displacement estimated using speckle tracking, could be due to a large decorrelation of the speckle pattern making it unrecognizable, or a large axial movement exceeding the bounds of the search region.

The decorrelation could be caused by a large lateral or elevational movement in the area. There are no apparent signs in the images, that either of the reasons mentioned above have occurred for the regions that show a poor correlation in image 4.23. The locations of the removed estimates seem to have random positions.

5.5 Freehand palpation

The elasticity phantom used for testing was described in section 3.3.3. When testing the algorithm on the elasticity phantom, the compression was created by manually applying force to the top surface of the phantom with the ultrasound transducer. There are several limits to this freehand palpation procedure.

Manually inducing the stress produces large insecurities in the uniformity of the force, as well as the risk of giving the transducer a slight change in angle when imaging. That would cause a misalignment of the pre- and post deformed echo frames, and thereby change the speckle pattern between two subsequent frames.

Doyley et al. (2001) compared the performance of freehand palpation to mechanically induced transducer motion. They found that the quality of the freehand elastograms were sufficient for clinical use, but highly dependent on the skill of the operator to maintain the appropriate strain rate. Seeing as the author is no skilled operator, using freehand palpation was perhaps not an optimal test.

A better way to compress the phantom would be to use a robotical arm that would compress the phantom with the same force, at the same angle every time and with the same period.

The elasticity phantom was confined by a hard box in all other surfaces than the top. Therefore it was difficult to induce much lateral displacement when compressing from the top. A solution could have been to remove one of the sides of the box to apply force to the side of the phantom while imaging from the top. Due to time limitations of the project, this test was not performed but could be tested in future work.

5.6 Speckle pattern decorrelation

The speckle tracking method is based on the assumption that the speckle pattern remains fairly stable when the tissue is displaced. This is a valid assumption when tissue is only displaced and the displacements are small, (Wells and Liang (2011)). But when deformation, noise and out-of-plane motion of the tissue is present it may cause the pattern to change.

As the pattern deteriorates, the tracking precision becomes poorer. If the pattern deteriorates too much, tracking will become impossible, as seen for the simulated images in the lateral direction.

5.7 Implications

There are several examples of elastography (with a varying method of compression) used in the field of brain imaging. Xu et al. (2013) used elastography to detect stiffness changes in brain tissue after stroke, and Scholz et al. (2004) investigated the use of ultrasound vibrography on swine brains during neurosurgery. Thus the applicability of elastography as an imaging modality useful for the brain has several validations.

This project, though, was intended as a step in the research towards using strain imaging during neurosurgery, by using speckle tracking as the method of displacement estimation. (Ultrasound in neurosurgery was presented in section 1.1.2). For this application the compression is enforced by the natural pulsation of the arteries. Thus the rest of this short section will present the already documented applications of speckle tracking as well as some implications for the future.

Speckle tracking was intended as a method of blood velocity estimation, that could overcome the limitations of Doppler imaging when it was introduced by Trahey et al. (1987), as one of the first in the field. Over the years speckle tracking has found numerous applications in other fields as well. Especially in cardiology where the technique is used to track the movement of different structures in the heart, such as the work done by Kaluzynski et al. (2001), to identify non-contracting regions of the *myocardium*.

After elastography was introduced by Ophir et al. (1991), speckle tracking has been applied in estimating tissue elasticity as well. Among others, Brusseau et al. (2014) performed strain imaging on breast lesions using a two dimensional speckle tracking method to generate the displacement matrix. Thus the usefulness of speckle tracking is well documented.

The key assumption in brain strain imaging using the natural pulsation as the deforming force is that the natural pulsation induces enough stress for the displacement to be measurable. This assumption has been validated by Selbekk et al. (2005). As explained by Amar et al. (2011); blood in the brain follows the cycle of the heart and due to the fixed volume of the scull, the changing of the volume of blood results in movement in the brain tissue.

Several studies on the possibility of using a two-dimensional speckle tracking method to generate strain images during neurosurgery have been published (Chakraborty et al. (2012) and Uff et al. (2009)). The latter investigated the usefulness and accuracy of real-time elastography in neurosurgery on brain and spine. The elastograms were compared to the professional opinion of the surgeon, and the results showed a good agreement between surgical findings and elastographic data. They thus deemed elastography useful for neurosurgeons.

As for this particular speckle tracking method developed during this project, there are several tests to be performed before it is possible to give a conclusion on the performance of the method, especially in the lateral direction, but the future for the speckle tracking method in the field of (brain) strain imaging during neurosurgery looks bright.

Chapter 6

Conclusion

Ultrasound strain imaging is an imaging modality that estimates and displays the differences in tissue stiffness. Two dimensional strain imaging has been the main focus of this thesis.

The main goals set for this thesis were to investigate previous methods of 2D strain estimation, implement one or several solutions in MATLAB, and evaluate the performance based on synthetic data and real data of an elasticity phantom.

Strain is generated from a matrix of displacement estimates. Thus finding a method to estimate two-dimensional displacement was the first challenge of the project. From a study of the different methods presented in the literature, it was chosen to implement a two-dimensional speckle tracking method. The reason for the choice was that the speckle tracking method was well documented in the literature and that it seemed to be a reasonably simple method to implement.

The strain estimator chosen for implementation was the central differences (CD) estimator.

The method was then tested on images that were simulated using Field II (Jensen and Svendsen (1992)), as well as images acquired of an elasticity phantom that contained inclusions isoechoic with the background but of different stiffness from the background.

To help with the analysis of the results, a graphical user interface (GUI) was developed. Implemented in the GUI were functions to give the user the possibility of optimizing speckle tracking and strain parameters in a simple way, as well as displaying the ultrasound images in a cineloop.

The results have shown that the developed method is able to estimate the strain and displacement of a movement in the axial direction with a high precision, even for subsample displacement.

The results from in the lateral direction have been more varying. This was expected from the theory due to the coarse resolution in the lateral direction, but both due to some challenges with the simulated images and time limitations in regard to testing the method

properly with the elasticity phantom; it is difficult to give a clear conclusion about the performance of the method in the lateral direction.

Nevertheless, a speckle tracking method that shows a promising ability of estimating axial and lateral displacement and strain has been developed. A hope is that the GUI developed will be a useful tool for the continuation of this project.

6.1 Suggestions for future work

Improvements on the developed lateral strain imaging algorithm:

As future work, it would be interesting to perform more tests on the ability of the method to estimate lateral strain. A suggestion would be to test a phantom that had the possibility of being compressed on one of the sides, thereby inducing a pure lateral movement. If it were to perform well for the lateral displacement estimation, it would be interesting to estimate strain with a more robust estimator as mentioned in section 5.3.2.

Imaging a phantom is an ideal situation, and seeing as there are already challenges in the lateral direction using an elasticity phantom, testing the method using clinical may be difficult. But clinical data is the ultimate goal and it would therefore be interesting to see how at least the axial tracking and strain estimation would perform.

If the method is to be used in real time, measures have to be taken to speed up the computation time of the displacement estimation. Some suggestions to speed up the search can be found in Zahiri-Azar and Salcudean (2006), who limits the search to specific areas within the search region based on previous estimates. Another suggestion would be to apply an iterative coarse-to-fine search method, which searches for the coarse displacement and thereafter divides the search region in half and finds the more accurate displacement estimate, Lopata et al. (2009).

Other methods of 2D strain imaging

In section 2.5 three other methods for estimating lateral displacement were presented. They have different approaches to lateral displacement estimation and thus comparing those methods to the one created in this project would be very interesting. The synthetic lateral phase (SLP) method would seem like a good first choice because after creating the synthetic lateral phase, speckle tracking was used to determine the displacements. Thus the method could probably be implemented without making too many changes to the method already developed.

Three dimensional strain imaging

An obvious limitation of estimating the strain in two dimensions is that the movement of a three-dimensional target is often three-dimensional. Thus to fully characterize the motion of the target, strain should be estimated in three-dimensions. Another incentive is that as lateral movement decorrelates the axial signal, out-of-plane motion deteriorates the estimation of movement in the axial and lateral direction.

Bibliography

Amar, M., Ternifi, R., Remenieras, J., 2011. Brain tissue motion estimation: 2d speckle tracking using synthetic lateral phase technique. pp. 123–126.

Bohs, L., Geiman, B., Anderson, M., Gebhart, S., Trahey, G., 2000. Speckle tracking for multi-dimensional flow estimation. Ultrasonics 38 (1), 369–375.

Børstad, T. K., 2010. Comparison of three ultrasound velocity estimators for strain imaging of the brain. Master's thesis, NTNU.

Børstad, T. K., 2011. Intraoperative strain imaging of brain tumors. Master's thesis, NTNU.

Brusseau, E., Detti, V., Coulon, A., Maissiat, E., Boublay, N., Berthezène, Y., Fromageau, J., Bush, N., Bamber, J., 2014. In vivo response to compression of 35 breast lesions observed with a two-dimensional locally regularized strain estimation method. Ultrasound in Medicine and Biology 40 (2), 300–312.

Chakraborty, A., Bamber, J., Dorward, N., 2012. Preliminary investigation into the use of ultrasound elastography during brain tumour resection. Ultrasound 20 (1), 33–40.

Chen, X., Zohdy, M., Emelianov, S., O'Donell, M., 2004. Lateral speckle tracking using synthetic lateral phase. IEEE transactions on ultrasonics, ferroelectrics, and frequency control 51 (5), 540–550.

Doyley, M., Bamber, J., Fuechsel, F., Bush, N., 2001. A freehand elastographic imaging approach for clinical breast imaging: System development and performance evaluation. Ultrasound in Medicine and Biology 27 (10), 1347–1357.

Hansen, H., Lopata, R., De Korte, C., 2009. Noninvasive carotid strain imaging using angular compounding at large beam steered angles: Validation in vessel phantoms. IEEE Transactions on Medical Imaging 28 (6), 872–880.

Hansen, H., Lopata, R., Idzenga, T., De Korte, C., 2010. Full 2d displacement vector and strain tensor estimation for superficial tissue using beam-steered ultrasound imaging. Physics in Medicine and Biology 55 (11), 3201–3218.

Hein, I., O'Brien, W. D., 1993. Current time-domain methods for assessing tissue motion by analysis from reflected ultrasound echoes. a review. IEEE Transactions on Ultrasonics, Ferroelectrics, and Frequency Control 40 (2), 84–102.

Jagannathan, J., Sanghvi, N., Crum, L., Yen, C.-P., Medel, R., Dumont, A., Sheehan, J., Steiner, L., Jolesz, F., Kassell, N., 2009. High-intensity focused ultrasound surgery of the brain: Part 1-a historical perspective with modern applications. Neurosurgery 64 (2), 201–210.

Jensen, J. A., Svendsen, N. B., 1992. Calculation of pressure fields from arbitrarily shaped, apodized, and excited ultrasound transducers. IEEE Transactions on Ultrasonics, Ferroelectrics, and Frequency Control 39 (2), 262–267.

Kallel, F., Ophir, J., 1997. A least-squares strain estimator for elastography. Ultrasonic Imaging 19 (3), 195–208.

Kaluzynski, K., Chen, X., Emelianov, S., Skovoroda, A., O'Donnell, M., 2001. Strain rate imaging using two-dimensional speckle tracking. IEEE Transactions on Ultrasonics, Ferroelectrics, and Frequency Control 48 (4), 1111–1123.

Konofagou, E., Ophir, J., 1998. A new elastographic method for estimation and imaging of lateral displacements, lateral strains, corrected axial strains and poisson's ratios in tissues. Ultrasound in Medicine and Biology 24 (8), 1183–1199.

Langeland, S., D'hooge, J., Torp, H., Bijnens, B., Suetens, P., 2002. A simulation study on the performance of different estimators for two-dimensional velocity estimation. In: Ultrasonics Symposium, 2002. Proceedings. 2002 IEEE. Vol. 2. pp. 1859–1862 vol.2.

Langeland, S., D'Hooge, J., Torp, H., Bijnens, B., Suetens, P., 2003. Comparison of time-domain displacement estimators for two-dimensional rf tracking. Ultrasound in Medicine and Biology 29 (8), 1177–1186.

Lopata, R., Nillesen, M., Hansen, H., Gerrits, I., Thijssen, J., de Korte, C., 2009. Performance evaluation of methods for two-dimensional displacement and strain estimation using ultrasound radio frequency data. Ultrasound in Medicine and Biology 35 (5), 796–812.

Ophir, J., Alam, S., Garra, B., Kallel, F., Konofagou, E., Krouskop, T., Varghese, T., 1999. Elastography: Ultrasonic estimation and imaging of the elastic properties of tissues. Proceedings of the Institution of Mechanical Engineers, Part H: Journal of Engineering in Medicine 213 (3), 203–233.

Ophir, J., Céspedes, I., Ponnekanti, H., Yazdi, Y., Li, X., 1991. Elastography: A quantitative method for imaging the elasticity of biological tissues. Ultrasonic Imaging 13 (2), 111–134.

Parker, K., Doyley, M., Rubens, D., 2011. Imaging the elastic properties of tissue: the 20 year perspective. Physics in medicine and biology 56 (1), R1–R29.

Prof. Bjørn A. J. Angelsen, P. H. G. T., 2010. Forelesningsnotater. Department of Circulation and Medical Imaging.

Purkayastha, S., Sorond, F., 2012. Transcranial doppler ultrasound: Technique and application. Seminars in Neurology 32 (4), 411–420.

Righetti, R., Srinivasan, S., Ophir, J., 2003. Lateral resolution in elastography. Ultrasound in Medicine and Biology 29 (5), 695–704.

Scholz, M., Fricke, B., Mönnings, P., Brendel, B., Schmieder, K., Siebers, S., Von Düring, M., Ermert, H., Harders, A., 2004. Vibrography: First experimental results in swine brains. Minimally Invasive Neurosurgery 47 (2), 79–85.

Selbekk, T., Bang, J., Unsgaard, G., 2005. Strain processing of intraoperative ultrasound images of brain tumours: Initial results. Ultrasound in Medicine and Biology 31 (1), 45–51.

Selbekk, T., Brekken, R., Solheim, O., Lydersen, S., Hernes, T., Unsgaard, G., 2010. Tissue motion and strain in the human brain assessed by intraoperative ultrasound in glioma patients. Ultrasound in Medicine and Biology 36 (1), 2–10.

Solheim, O., Selbekk, T., Jakola, A., Unsgård, G., 2010. Ultrasound-guided operations in unselected high-grade gliomas-overall results, impact of image quality and patient selection. Acta Neurochirurgica 152 (11), 1873–1886.

Souchon, R., Rouvière, O., Gelet, A., Detti, V., Srinivasan, S., Ophir, J., Chapelon, J.-Y., 2003. Visualisation of hifu lesions using elastography of the human prostate in vivo: Preliminary results. Ultrasound in Medicine and Biology 29 (7), 1007–1015.

Stepanishen, P. R., 1971a. The time-dependent force and radiation impedance on a piston in a rigid infinite planar baffle. J. Acoust. Soc. Am. 49, 841–849.

Stepanishen, P. R., 1971b. Transient radiation from pistons in an infinite planar baffle. J.Acoust.Soc.Am. 49, 1629–1638.

Techavipoo, U., Chen, Q., Varghese, T., Zagzebski, J., 2004. Estimation of displacement vectors and strain tensors in elastography using angular insonifications. IEEE Transactions on Medical Imaging 23 (12), 1479–1489.

Trahey, G., Allison, J., Von Ramm, O., 1987. Angle independent ultrasonic detection of blood flow. IEEE Transactions on Biomedical Engineering 34 (12), 965–967.

Trahey, G., Hubbard, S., Von Ramm, O., 1988. Angle independent ultrasonic blood flow detection by frame-to-frame correlation of b-mode images. Ultrasonics 26 (5), 271–276.

Tupholme, G. E., 1969. Generation of acoustic pulses by baffled plane pistons. Mathematika 16, 209–224.

Uff, C., Garcia, L., Fromageau, J., Dorward, N., Bamber, J., 2009. Real-time ultrasound elastography in neurosurgery.

Walter, U., 2012. Transcranial sonography of the cerebral parenchyma: Update on clinically relevant applications. Perspectives in Medicine 1-12, 334–343.

Wells, P., Liang, H.-D., 2011. Medical ultrasound: Imaging of soft tissue strain and elasticity. Journal of the Royal Society Interface 8 (64), 1521–1549.

Xu, Z., Lee, R., Chu, S., Yao, A., Paun, M., Murphy, S., Mourad, P., 2013. Evidence of changes in brain tissue stiffness after ischemic stroke derived from ultrasound-based elastography. Journal of Ultrasound in Medicine 32 (3), 485–494.

Zahiri-Azar, R., Salcudean, S., 2006. Real-time estimation of lateral displacement using time domain cross correlation with prior estimates. Vol. 1. pp. 1209–1212.

Appendices

Appendix A

Matlab Code

The .m files of the calculations are added to this appendix, the estimation functions and their parameters.

A.1 Speckle Tracking

A.1.1 Normalized correlation search

```
1  function [axDispArray, latDispArray, cDispArray] =
       speckleTrackingNormxcorr2(X,pST, centerArray)
2              % speckleTrackingNormxcorr2 calculates the
                   axial, axDispArray,
3              % and lateral, latDispArray, displacement
                   matrices of two
4              % subsequent images, X. cDispArray is the
                   correlation matrix of
5              % the correlation searches.
6
7              % centerArray defines the points the kernels
                   are centered
8              % around.
9
10             kernelSize = pST.kernelSize;
11             maxLag = pST.maxDisplacement;
12
13             ref = real(X(:,:,1));
14             displaced = real(X(:,:,2));
15
16             axDispArray = zeros(size(centerArray,1), size(
                   centerArray,2));
```

```
17              latDispArray = zeros(size(centerArray,1), size(
                    centerArray,2));
18              cDispArray = zeros(size(centerArray,1), size(
                    centerArray,2));
19
20              if(size(displaced,1) > 1)
21                  for j = 1:size(centerArray,1)
22                      disp(['center( ',num2str(j)]);
23                      for k = 1:size(centerArray,2)
24
25
26                          c = centerArray{j,k};
27
28                          template = ref(c(1)-kernelSize(1):c
                                (1)+ kernelSize(1),...
29                              c(2)-kernelSize(2):c(2)+
                                    kernelSize(2));
30
31                          search_region = displaced((c(1)-
                                kernelSize(1)-maxLag(1)):(c(1)+
                                kernelSize(1)+ maxLag(1)),...
32                              (c(2)-kernelSize(2)-maxLag(2))
                                    :(c(2)+kernelSize(2)+maxLag
                                    (2)));
33
34                          cc = normxcorr2(template,
                                search_region);
35                          ccred = cc((1+end)/2+(-maxLag(1):
                                maxLag(1)),(1+end)/2+(-maxLag(2)
                                :maxLag(2)));
36                          [m, ind] = max(abs(ccred(:)));
37
38
39                          [zpeak, xpeak] = ind2sub(size(ccred
                                ), ind);
40
41                          % interpolation axial and lateral
42                          latInterpol = 0.00001;
43                          axInterpol = 0.0001;
44                          if m < 0.9999
45
46                              if xpeak > 1 && xpeak < (size(
                                    ccred,2)-1)
47                                  latVal = ccred(zpeak, [
                                        xpeak-1,xpeak,xpeak+1]);
```

```
48                                  latIntVal(1,:) = (xpeak-1):
                                        latInterpol:(xpeak+1);
49                                  latIntVal(2,:) = interp1([
                                        xpeak-1, xpeak, xpeak
                                        +1], latVal, latIntVal
                                        (1,:), 'spline');
50                                  [lmaxInt, lintInd] = max(
                                        abs(latIntVal(2,:)));
51                              else
52                                  lmaxInt = 0;
53                              end
54
55                              if zpeak > 1 && zpeak < (size(
                                    ccred,1)-1)
56                                  axVal = ccred([zpeak-1,zpeak
                                        ,zpeak+1], xpeak)';
57                                  axIntVal(1,:) = (zpeak-1):
                                        axInterpol:(zpeak+1);
58                                  axIntVal(2,:) = interp1([
                                        zpeak-1, zpeak, zpeak+1],
                                         axVal, axIntVal(1,:), '
                                        spline');
59                                  [amaxInt, aintInd] = max(
                                        axIntVal(2,:));
60                              else
61                                  amaxInt = 0;
62                              end
63
64                               if lmaxInt > m && lmaxInt >
                                     amaxInt
65                                   xpeak = latIntVal(1,lintInd
                                         );
66                                   m = lmaxInt;
67                                   if amaxInt > m
68                                       zpeak = axIntVal(1,
                                            aintInd);
69                                   end
70
71                               elseif amaxInt > m && amaxInt >
                                     lmaxInt
72                                   zpeak = axIntVal(1, aintInd
                                         );
73                                   m = amaxInt;
74                                   if lmaxInt > m
```

```
75                                          xpeak = latIntVal(1,
                                                lintInd);
76                                      end
77                                  end
78
79                              end
80
81                              cDispArray(j,k) = m;
82                              axDispArray(j,k) = zpeak - (maxLag
                                    (1)+1);
83                              latDispArray(j,k) = xpeak - (maxLag
                                    (2)+1);
84
85                          end
86                      end
87                  end
88  end
```

A.1.2 Speckle Tracking Parameters

```
1  classdef SpeckleTrackParams
2      %SPECKLETRACKPARAMS Summary of this class goes here
3      %   Detailed explanation goes here
4
5
6
7      properties
8          kernelSize = [60 5];
9          maxDisplacement = [20 4];
10         kernelOverlap = []; % percent overlap between
               kernels axially and laterally
11         origZ = [];
12         origX = [];
13         stepSize = [20 2];
14         %position of rectangular ROI for GUI
15         rectPosition = [0 0 0 0];
16     end
17
18     methods
19         function x = xLost(obj)
20             x = obj.kernelSize(2) + obj.maxDisplacement(2);
21         end
22         function y = yLost(obj)
23             y = obj.kernelSize(1) + obj.maxDisplacement(1);
24         end
25     end
```

```
26
27 end
```

A.2 Strain estimation

A.2.1 Central difference strain estimation

```
1  function [axS, latS, axS_C, latS_C] = strainEstimatorRt(axD
       , latD, C, pA, pST)
2  %STRAINESTIMATOR  The strain estimator is based on the
       central difference theorem. A
3  %    vector, (h,k) is convolved with the displacement matrix
        to produce the
4  %    strain image.
5  %
6  % axD, latD are the axial and lateral displacement matrices
       , respectively.
7  % C is the correlation coefficient matrix
8  % pA and pST are structs containing the parameters of the
       strain
9  % estimation.
10 % axS and latS are the estimated strain matrices.
11 % axS_C and latS_C are the axial and lateral correlation
       matrices
12 % respectively.
13
14 axDelta_m  = pA.dAx;
15 latDelta_m = pA.dLat;
16 stepSize = pST.stepSize;
17
18 %% Axial strain
19 h             = zeros(axDelta_m + 1,1);
20 h(1) = (1/(axDelta_m*stepSize(1)));
21 h(axDelta_m+1) = -1/(axDelta_m*stepSize(1));
22
23 h_c             = zeros(axDelta_m + 1, 1);
24 h_c(1)          = 1/2;
25 h_c(axDelta_m+1) = 1/2;
26
27 axS = conv2(axD, h, 'valid');
28 axS_C = conv2(C, h_c, 'valid');
29
30
31 %% Lateral strain
32 k             = zeros(1,latDelta_m + 1);
33 k(1)          = 1/(latDelta_m*stepSize(2));
```

```
k(latDelta_m+1) = -1/(latDelta_m*stepSize(2));

k_c             = zeros(1,latDelta_m + 1);
k_c(1)          = 1/2;
k_c(latDelta_m+1) = 1/2;


latS = conv2(latD, k, 'valid');
latS_C = conv2(C, k_c, 'valid');
```

A.2.2 Strain Estimation Parameters

```
classdef StrainEstParam
    % Parameters used by the velocity estimators

    properties
        dAx = 2;
        dLat = 2;
        dy = 3;
        method = 'Normal';
    end

    methods
        function ax = axLost(obj)
            ax=obj.dAx;
        end
        function lat = latLost(obj)
            lat = obj.dLat;
        end
        function x = xLost(obj)
            if strcmp(obj.method,'Sobel')
                                x=obj.dy-1;

            else
                                x=0;

            end
        end
    end
end
```

Appendix B

Tables

This appendix contains the tables with information about: the simulation; imaging system and phantom parameters, the simulated data-sets presented in section 4.1 and phantom images presented in section 4.2; estimation parameters.

B.1 Simulated images

B.1.1 Simulated phantom parameters

Table B.1: Parameters of simulated phantom

Symbol	Value	Description
Δ x	40mm	Width of phantom in x-direction
Δ y	40mm	Width of phantom in y-direction
Δ z	90mm	Depth of phantom
z-start	30mm	Start of phantom surface
N	50 000	Number of scatterers in image

B.1.2 Simulated imaging parameters

Table B.2: Imaging parameters of simulated images

Symbol	Value	Description
f_0	10MHz	Center of transmit frequency
f_s	100MHz	Sampling frequency of RF-data
c	1540m/s	Speed of sound
λ	$\frac{c}{f_0}$	Wavelength of transmit pulse
kerf	$\frac{\lambda}{20}$	Space between elements
$N_{elements}$	192	Number of physical elements of aperture
N_{active}	64	Number of active elements of aperture
N_{lines}	50	Number of A-lines in image
D	10	Decimation factor from RF-data to B-mode image
Δ x	40mm	Width of image
Δ z	75 mm	Depth of image
z_{start}	35mm	starting depth of image

B.1.3 Displacement parameters from section 4.1

Table B.3: Coordinates of tracked points and displacement amplitudes for simulated data-set 1

Point	Coordinates	Amplitude [mm]	Amplitude [samples]
Point 1	[270, 128]	$\pm$ 0.1	$\pm$ 13
Point 2	[900, 128]	$\pm$ 0.2	$\pm$ 26
Point 3	[1550, 128]	$\pm$ 0.5	$\pm$ 65
Point 4	[2100, 128]	$\pm$ 0.6	$\pm$ 78
Point 5	[2750, 128]	$\pm$ 0.7	$\pm$ 91
Point 6	[3400, 128]	$\pm$ 0.8	$\pm$ 104
Point 7	[4150, 128]	$\pm$ 0.9	$\pm$ 117
Point 8	[4800, 128]	$\pm$ 1	$\pm$ 130
Point 9	[5300, 128]	$\pm$ 0	$\pm$ 0

Table B.4: Limitations of speckle tracking method

Point	Amplitude [mm]	Amplitude [samples]
Curve 1	± 0.1	± 13
Curve 2	± 0.09	± 11.7
Curve 3	± 0.085	± 11.05
Curve 4	± 0.065	± 8.45
Curve 5	± 0.04	± 5.2
Curve 6	± 0.01	± 1.3
Curve 7	± 0.009	± 1.17
Curve 8	± 0.0085	± 1.105
Curve 9	± 0.0065	± 0.845
Curve 10	± 0.005	± 0.650
Curve 11	± 0.004	± 0.520
Curve 12	± 0.001	± 0.130
Curve 13	± 0.0005	± 0.065
Curve 14	± 0.0001	± 0.013

Table B.5: Coordinates of tracked points and displacement amplitudes for simulated data-set 3

Point	Coordinates	Amplitude [mm]	Amplitude [samples]
Point 1	[3000, 30]	± 2	± 17
Point 2	[3000, 70]	± 1.5	± 12
Point 3	[3000, 110]	± 1	± 8.5
Point 4	[3000, 150]	± 0.7	± 6
Point 5	[3000, 190]	± 0.6	± 5.12
Point 6	[3000, 220]	± 0.5	± 4.26

B.2 Phantom images

Table B.6: Parameters of the strain and displacement estimation for the elasticity phantom images

Symbol	Value	Description
I_ax	10000	Number of new samples axially
I_lat	100000	Number of new samples laterally
K	[60 5]	Kernel size [samples lines]
M	[20 4]	Maximum lag [samples lines]
S	[5 1]	Step size [samples lines]
dAx	60 * 5	Axial strain estimation segment length
dLat	5	Lateral strain estimation segment length

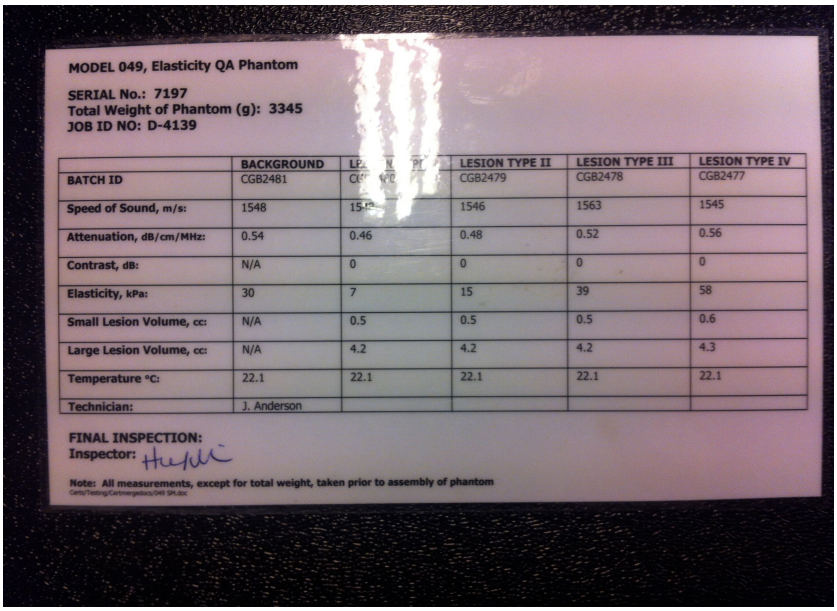

Figure B.1: An image of the properties of the elasticity phantom, which specifies the speed of sound and Young's modules, etc., of the different inclusions.